Probing the vertical abundance structure of the Galactic disc using red clump stars

Gaël Noirot

Lund Observatory
Lund University

2014-EXA86

Degree project of 30 higher education credits (for a degree of Master)
June 2014

Supervisor: Thomas Bensby
Assistant supervisor: Gregory Ruchti

Lund Observatory
Box 43
SE-221 00 Lund
Sweden

Acknowledgements

I am really grateful to my supervisor, Thomas Bensby, first for putting his trust in me in allowing me to work on this fascinating project (and doing so, letting me prolong my stay in Lund), also for the regular help that allowed me to progress and finish on time, and also for the numerous draft readings and corrections (+ the swedish translation, tack så mycket!). I also want to thank Gregory Ruchti, my assistant-supervisor, for the precious advice and guidance he gave me throughout the 20 weeks of this work as well as for draft proofreadings.

I also want to thank Anders Johansen, who is greatly responsible for having put me on the tracks of this project.

Also, I want to thank here Anne-Sophie Cordan and Ariane Lançon for their valued guidance when I was planning to go to Lund for a student mobility.

And last but not least, I want to thank all my officemates for the peaceful working atmosphere that never vanished.

Abstract

Context. Dwarf stars have been extensively used as probes in the solar neighbourhood for improving our picture of the stellar populations' distributions inside the Milky Way. Of particular utility is to look for observational evidences of two distinct stellar populations characteristic of their affiliation to two distinguishable zones of the Milky Way: the thin and the tick disc. Indeed, three decades ago an observational evidence of two distinct stellar populations in the vertical structure of our galaxy was discovered. Since then, significant data have been obtained in the solar neighbourhood and showed that thick disc stars are more metal-poor, α-enhanced, older, rotationally lagging behind the sun, and have greater peculiar velocities than thin disc stars in average. Nevertheless, most distant regions are essentially non-explored since dwarf stars become too faint to to be observed with high resolution spectrographs. However, red clump stars can be used in order to probe the Milky Way farther than the solar neighbourhood as they provide sufficient luminosity and preserved photospheres.
Aims. With high-resolution spectra of 43 red clump stars located $\sim$200 to 700 parsecs away from the sun in the direction of the north galactic pole, obtained with the MIKE echelle spectrograph during two observing runs in 2008 and 2009, this study aims at looking whether the two population trends persist outside the solar neighbourhood.
Methods. The elemental abundances of the stars are determined from the measurement of the spectral lines' equivalent widths and fitting of Kurucz model photosphere under 1-D LTE assumption. Dust maps are used to compute the stars' distances; their space velocities are calculated, and their orbital properties computed using a Paczyński potential.
Results. The majority of our stars have cold peculiar velocities (under 50 km/s with respect to the sun) and 9 have warm peculiar velocities (over 100 km/s). Investigations in e (eccentricities) and zmax (maximum height) according to α-enhancement show that low e or low zmax stars are confined near solar metallicity with [Fe/H] not below -0.3 dex, and they show a non-α-enhanced $\sim$flat trend in α-elements versus metallicity. However, high e or high zmax stars are more metal poor with one star reaching -1.5 dex in [Fe/H], and they show first an increasing slope in α-enhancement with decreasing metallicity and then a $\sim$flat α-enhanced region at poor metallicity ([Fe/H] < -0.5 dex). The warm stars all belong to the later trends whereas almost all cold stars belong to the first trend. Moreover, we find an increasing α-enhancement and decreasing metallicity as we select stars rotationally lagging behind the sun.
Conclusions. Our results demonstrate that the abundance trends seen locally, and distinguishing the thin and the thick disc of the Milky Way, most likely persist outside the solar neighbourhood.

Populärvetenskaplig sammanfattning

Astrofysiker har fortfarande inte kunnat enats om ett unikt scenario för hur vår galax Vintergatan bildats och utvecklats. De senaste decennierna har flera scenarier framkommit och som i enlighet med nya observationer och upptäckter av vår Vintergatas fördelning av stjärnor, andra galaxers former, delvis kan förklara observationerna.

Speciellt intressanta för Vintergatan är långlivade sollika dvärgstjärnor vars atmosfärer har behållit den kemiska sammansättning som de gasmoln de en gång bildades från hade. Dessa ljussvaga stjärnor har studerats i stor utsträckning i solens närhet (inom ca 100 pc från solen) för att spåra den kemiska utvecklingen av Vintergatan. De stora tekniska framstegen av rymd- och markbaserade teleskop och instrument, har tillåtit oss att på senare tid observera, med stor noggrannhet, stjärnor som ligger betydligt längre bort. I synnerhet röda klumpstjärnor, som är betydligt mer ljusstarka än sollika dvärgstjärnor, och vars atmosfärer också till stor del har bevarat de kemiska signaturerna från när de bildades. Vidare är den absoluta ljusstyrkan hos röda klumpstjärnor inte beroende på massa eller ålder, men uppvisar ett beroende på färg och metallicitet, som har kalibrerats. De kan således användas som avståndsindikatorer för de strukturer de befinner sig i. Då de även är bra indikatorer av den kemiska sammansättningen av deras födelseplatser, och då det är förhållandevis enkelt att mäta deras kinematiska egenskaper, gör att röda klumpstjärnor är speciellt bra lämpade för denna studie som ämnar att öka vår kunskap om Vintergatan utanför solens omedelbara närhet.

Av särskilt intresse för detta arbete är att leta efter observationella bevis på två olika stjärnpopulationer i Vintergatans skiva, eller disk: den tunna och tjocka disken, som upptäcktes för tre decennier sedan i en studie av den vertikala strukturen i vår galax. Sedan dess har det visat sig att tjocka diskstjärnor är mer metallfattiga, har högre halter av alfa-grundämnena, de är äldre, och roterar långsammare i solen i sina banor kring Vintergatans cenrum, samt har i allmänhet en större total hastighet (radiell och vertikal), än tunna diskstjärnor.

Denna studie ämnar att undersöka om dessa två diskpopulationer som man kan se i solens närhet även existerar längre bort från solen. Med hjälp av högupplösta spektra av 43 röda klumpstjärnor som är belägna ungefär 200-700 parsecs bort från solen i riktning mot norra galaktiska polen, observerade med echellespektrografen MIKE under två observerationsrundor i 2008 och 2009, så har vi bestämt ymnigheter av olika grundämnen i stjärnorna, beräknas deras avstånd, hastigheter, och galaktiska banparametrar.

Studien visar att en majoritet av stjärnorna i vårt urval har tunn disk-kinematik, samt att majoriteten av dessa stjärnor har kemisk sammansättning som är typisk för den tunna disken. De stjärnor som noterbart roterar långsammare än solen, eller sådana vars banor

är väldigt excentriska, eller om banan har stor maximal höjd (över eller under Galaktiska planet), uppvisar de typiska egenskaperna som observerats för den tjock skivan: järnhalter som i genomsnitt är lägre än solens samt höga halter av alfa-grundämnena (Ca, Mg, O, Si, Ti), jämfört med solen.

Våra resultat indikerar att de halttrender som observerats lokalt nära solen också existerar längre bort, och att dessa möjligtvis kan kopplas till de två stjärnpopulationerna som upptäckts i Vintergatans vertikala struktur: den tunna och tjocka disken.

Contents

Acknowledgements **iii**

Abstract **iv**

Populärvetenskaplig sammanfattning **v**

List of Figures **3**

List of Tables **4**

1 Introduction **5**

2 Context of the study **6**
2.1 Preamble 6
2.2 General context 6
2.3 The thin and the thick discs 7
2.4 Selection of the stars 9
2.5 Presentation of our data 10

3 Tools for spectra analyses **13**
3.1 IRAF 13
3.2 TAME 14
3.3 AMOOG 15

4 Abundances **17**
4.1 Determining the stellar abundances 17
4.1.1 Measuring the equivalent widths of the stars with TAME 17
4.1.2 Getting the abundances and atmospheric parameters with AMOOG . 18
4.1.3 Improving the results 20
4.1.4 HR diagram of our red clump stars 22
4.1.5 Stellar abundances 22
4.2 Inferring stellar chemical properties 23
4.2.1 Comparison to Mishenina et al. (2006) 23
4.2.2 Comparison to Bensby et al. (2014) 25
4.3 Conclusions 26

5 Kinematics **27**
5.1 Determining the stars' kinematics . . . 27
5.1.1 The SIMBAD database . . . 27
5.1.2 Radial velocity correction . . . 27
5.1.3 Getting the stars' distances . . . 28
5.1.4 Distance uncertainties . . . 30
5.1.5 Calculating the galactic space velocities of our stars . . . 31
5.1.6 Galactic orbits . . . 33
5.2 Inferring stars' dynamical properties . . . 33
5.2.1 Velocity distribution . . . 33
5.2.2 Positions . . . 35
5.2.3 Further investigation . . . 36
5.3 Conclusions . . . 36

6 Investigations **39**
6.1 Eccentricity . . . 39
6.2 Maximum height . . . 40
6.2.1 Visual investigation . . . 40
6.2.2 Refined approach . . . 42
6.3 Space velocity . . . 45
6.4 Conclusions . . . 45

7 Conclusion **47**

Bibliography **48**

A Abundances and stellar parameters **50**

B References to kinematics used **55**

C Kinematic properties of our stars **57**

List of Figures

2.1 Colour-magnitude diagram of Hipparcos stars 8
2.2 The Milky Way structure seen edge-on 9
2.3 Near infrared colour-magnitude diagram of stars towards the galactic poles . 10
2.4 Raw data from the CCD chip 11
2.5 Reduced spectra 12

3.1 IRAF user interface 14
3.2 TAME user interface 15

4.1 Diagram of an equivalent width 18
4.2 Distribution of the iron outliers removed 21
4.3 Change in stellar parameters after the first results' improvement 21
4.4 HR diagram 22
4.5 Plots of the abundances 24

5.1 Map of the star coordinates 29
5.2 Diagrams of space velocities 34
5.3 Galactic coordinates 35
5.4 Positions of the stars 37
5.5 Toomre diagram discerning group 1 and group 2 stars 38

6.1 α-abundances kinematically colour labelled 40
6.2 α-abundances with eccentricity 41
6.3 α-abundances with maximum height 42
6.4 Abundances versus height, refined approach 44
6.5 Abundances versus tangential velocity, refined approach 46

List of Tables

A.1 Abundances 50
A.2 Abundance uncertainties 52
A.3 Atmospheric parameters 54

B.1 References used for the relevant properties of our stars 55

C.1 Stars' distances and their uncertainties 57
C.2 Space velocities and their uncertainties 59
C.3 Galactic orbital parameters 60

Chapter 1

Introduction

Since the dawn of mankind people have looked at the sky and wondered about the origin of the moving objects they could see and the purpose of their recurrences. Nowadays, great technological improvements in observational astronomy allow us to look for scientifically consistent answers by probing with high accuracy these objects and farther away. Moreover, our galaxy the Milky Way, and particularly the solar neighbourhood, is the best laboratory for studying stellar populations since it is the unique place where all type of stars can be resolved with enough efficiency. This allow astronomers to infer models, reflecting the observations, about the formations and evolutions of stellar populations and galaxies.

During the past decades, astronomers discovered that many galaxies, including ours, presented two overlapping galactic discs instead of one, and whose apparent structures were distributed differently according to distance from the galactic plane. The question arose whether these two discs were intrinsically different, or were hosting the same stellar populations that only had shuffled over time. The solar neighbourhood became extensively studied, using long-lived stars as probes, to look for different chemical and kinematic behaviours in those two discs in an attempt to discern between them. Different behaviours were found, but the solar neighbourhood being a really small region inside the Milky Way, it appears necessary to extend the area of research and investigate outside the solar neighbourhood.

Therefore, this thesis aims at answering the following question: do the different chemical and kinematic trends seen locally and attributed to either the thin or the thick disc persist outside the solar neighbourhood? A detailed elemental abundance study using high-resolution spectra of 43 red clump stars is performed in order to answer this question. Abundances and kinematics are studied and correlations also investigated.

This report first present general concepts about the context of the study: its interests, the thin and the thick disc, and the data we rely on for our study, in chapter 2. We then briefly present the tools of spectra analyses we used to treat our data in chapter 3, before to explain how we determined the stellar parameters and abundances of our stars and infer chemical properties in chapter 4. Using the same structure in chapter 5, we explain how we determined the kinematics of our stars before to infer dynamical properties. Lastly, we investigate the relations between kinematics and abundances in chapter 6, and conclude in chapter 7.

Chapter 2

Context of the study

2.1 Preamble

Galaxies form from gas clouds that collapse in the cosmic web and whose gravitationally bound gas accretion starts to form a disc-like shape. This gas serves then to form the stars within their host galaxy. However, the processes forming galaxies and governing their evolutions leading to what we see today are complex and still not fully understood. Theories and simulations can be made but are only improved through observations. Actually, detailed and accurate observations not only help us to improve our picture of the galaxies as we see them today, but can serve to probe their origins and evolutions. Indeed, probing stars is a direct method to obtain information on the composition of the gas they formed form. Particularly, probing stars inside the different stellar components of the galaxies as we see them today (see figure 2.2): the galactic disc (some having a thin and a thick component that we investigate in this study), the bulge (central group of stars of high stellar concentration), and the halo (spherical component of low stellar concentration), gives hints into the different possible processes of formation and evolution. Do the stellar components have the same origins? Do they followed the same evolution processes? Do some of them originate from mergers or interactions with other galaxies? Those are among the questions that observations allow to investigate. Moreover, the Milky Way, our own galaxy, is the only galaxy where the type of stars that are still directly representative of the gas clouds they formed from can be resolved with high resolution. This is why the Milky Way is extensively studied in this field of research, and whose obtained results serve as a benchmark for general galaxy formation and evolution.

2.2 General context

Nowadays, astrophysicists still do not agree on a unique scenario regarding the formation, and evolution, of our galaxy the Milky Way. Indeed, several scenarios have been developed during the past decades and have evolved according to the new observations and discoveries of our current galaxy's stellar distributions, other galaxies' shapes, leading today to a few set of coherent theoretical scenarios that can explain in part the observations.

Thanks to the great technological improvements of space and ground-based telescopes and instrumentation, we are now able to observe with great accuracies stars farther than the solar neighbourhood. Therefore, astrophysicists are able to get a more accurate picture of the stellar populations' distributions inside the Milky Way, constraining the theoretical scenarios,

which can serve as a reference for general galaxy formation and evolution.

Of particular interest in the picture of the Milky Way is to look at long-lived stars whose photospheres (also called atmospheres) still hold the chemical signatures of the gas clouds they formed from. Indeed, the nuclear reactions of long-lived stars (also known as low-mass stars: between 0.5 and 2 solar masses) are currently confined in their cores and have not perturbed the chemical composition of their photospheres (outer layer), since those stars fuse hydrogen into helium in their core for approximately 10 Gyrs (or more for the lightest ones) which is close to the assumed age of the Milky Way (13 Gyrs). This is the reason why low-mass solar type stars in the solar neighbourhood have been extensively used to trace the chemical evolution of the Milky Way (e.g. Edvardsson et al., 1993, or Bensby et al., 2014 who explore the stellar disc by studying dwarf stars in the solar neighbourhood).

However, low-mass stars are also the faintest ones, hence they become too dim to be observed with high resolution spectrographs at high distances. Therefore, as we want to look farther away than the solar neighbourhood (roughly a heliocentric sphere of radius 100 pc[1]) to have a more complete picture of the Milky Way, we have to find a compromise between sufficient luminosity and preserved photospheres. This compromise is the red clump stars. Indeed, red clump[2] is the name given at low-mass stars when they reach the core helium burning phase of their evolution, after having left the main-sequence (stage of the hydrogen to helium fusion happening in the stars' core, also known as the proton-proton chain). So, even though they undergo heavier nuclear reaction chains than the proton-proton chain, the heavier elements of their outer layers and photospheres are still preserved since the nuclear reactions are confined in their inner layers. Moreover, they are much brighter than main-sequence low-mass stars, so both their chemical compositions and kinematics can be inferred with great accuracies from observations. Furthermore, their absolute magnitude does not depend on mass or age but shows a dependance on their colour and metallicity that has been been calibrated by Bilir et al. (2013). Thus, they are really good distance indicators of the structures they are in (for instance, see also Grocholski & Sarajedini (2002), who study the K-band magnitude of red clump stars as a distance indicator and calculate the distances of star clusters using this method). Being good tracers of the chemical composition of their natal region(s) and being likely to provide precise kinematic properties, red clump stars are the targets of this study as they will allow us to increase our knowledge about the Milky Way outside the solar neighbourhood.

2.3 The thin and the thick discs

Of particular interest in this work is to look for observational evidences of two distinct stellar populations characteristic of their affiliation to two distinguishable but overlapping zones of the Milky Way : the thin and the tick disc (see figure 2.2). Indeed, three decades ago an observational evidence of two distinct stellar populations in the vertical structure of our galaxy was discovered by Gilmore & Reid (1983). They showed that the distribution of stars below and above the Milky Way's plane was better fitted with two profiles rather than one, revealing that an "old disc" (now known as the thin disc) was dominant up to 1 kpc above or below the sun, while beyond this limit "an older, more metal-poor population is seen" (now

[1] 1 pc $\simeq 2 \cdot 10^5$ AU, where pc stands for parsec and AU for Astronomical Unit.

[2] This name has been given after the feature, on the colour-magnitude diagram, of these stars that are gathered ("clumped") in a really tiny range of magnitude and red colour (see figure 2.1).

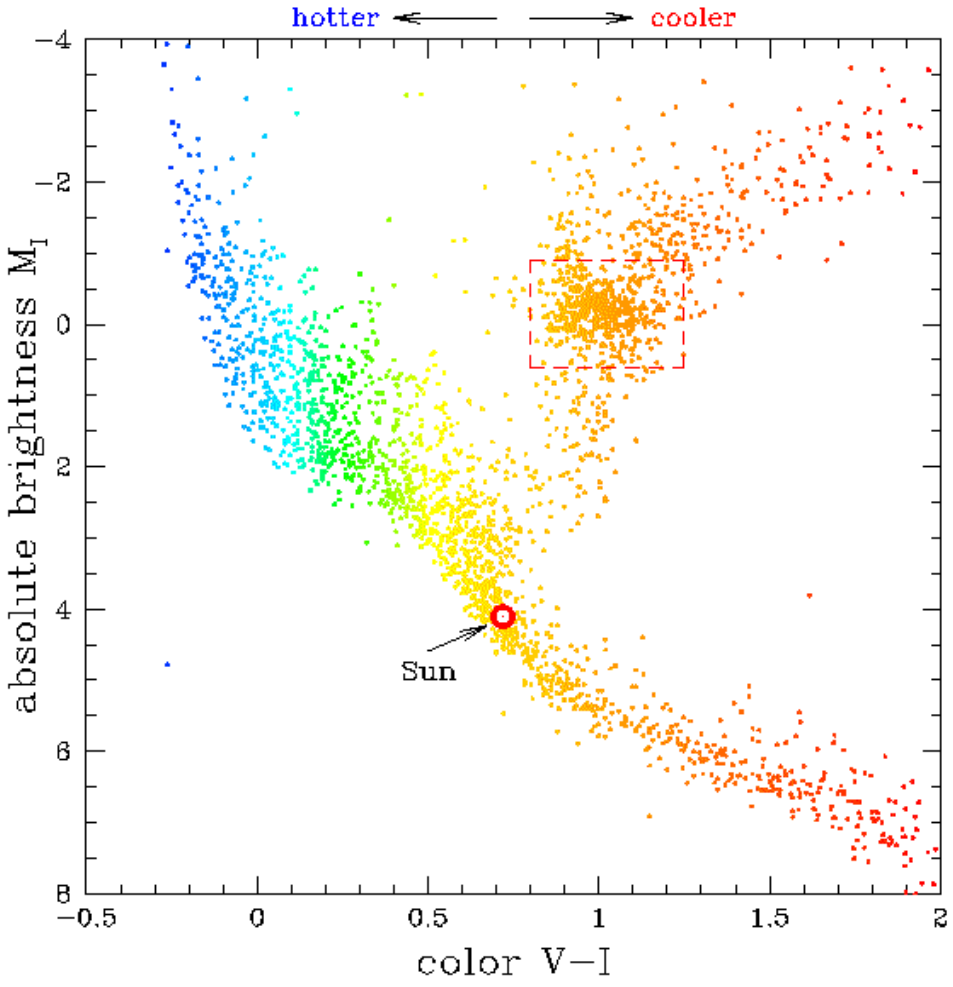

Figure 2.1: Colour-magnitude (or Hertzsprung-Russell) diagram of the stars from the Hipparcos catalogue. Red clump stars are confined in the red box. The abscissa of the diagram is the difference between visual (V) and near infrared (I) fluxes. The ordinate of the diagram is the absolute brightness (also known as absolute magnitude) in the I band. Reference: `http://www.astronomy.ohio-state.edu/~kstanek/CfA/RedClump/`.

known as the thick disc). Even though the interest for this area of study has risen in the last decade, the elemental abundance trends of the thin and thick discs have preferentially been inferred utilising long-lived dwarf stars in the solar neighbourhood and the results of the different studies were at this time rather conflicting (Feltzing et al., 2003). However, even if more recent works seem to agree and have studied the trends utilising high number of targeted dwarf stars (714 F and G dwarfs in Bensby et al., 2014, where abundance behaviours seem in agreement with Mishenina et al., 2006), the inner and outer regions of the disc and its vertical trends above or below the plane are still poorly studied, but can constrain the thick disc formation scenario and by extension the Milky Way formation one, giving a benchmark for galaxy formation.

Indeed, the different thick disc formation scenarios, summarised briefly in Feltzing et al. (2003) (from reference therein –Gilmore et al., 1989), lead to different age and abundance distributions for the thin and the thick disc, with nonetheless: the thick disc stars being more

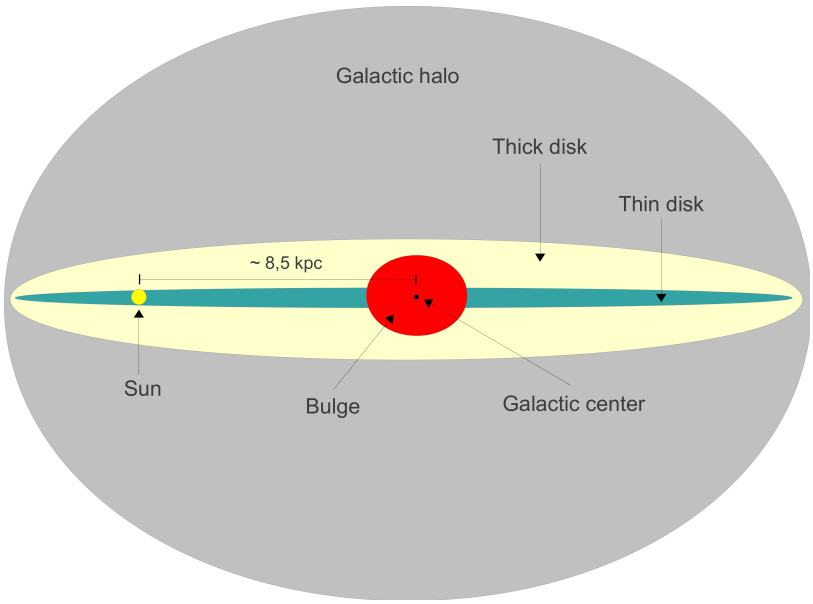

Figure 2.2: Representation of the thin and the thick disc of the Milky Way. The Bulge and Halo are also shown. Reference: `http://en.wikipedia.org/wiki/Thick_disk`.

metal-poor, α-enhanced, older, and having greater peculiar space velocities than the thin disc stars in average. Therefore, knowing today's abundance and age trends hint to the most likely formation scenario.

Based on our data, this study will allow us to confirm, or not, the persistence outside the solar neighbourhood of the two population trends of the Milky Way portrayed in many papers: the thin and the thick disc. Therefore, constraining formation and evolution scenarios of the Milky Way is a likely outcome of further analyses of the results of this study.

2.4 Selection of the stars

Red clump stars are confined in a small range of colour and magnitude, and are particularly distinct in the K and J bands. Thus, the stars have been targeted according to magnitude and colour in these bands. Figure 2.3 shows the near infrared (NIR) colour-magnitude diagram towards the poles where we can see three features. We can distinguish the foreground dwarf main sequence on the left, a vertical branch on the right representative of late type stars, and another vertical feature in the middle consisting of red clump stars. At high apparent magnitudes (low brightness) in the K band we see a confusion between the three populations. But, at lower apparent magnitude (higher brightness) than $K = 10$ and staying in a ± 0.2 mag range around the mean colour of the red clump stars allow to be free from contamination (Cabrera-Lavers et al., 2005). Therefore, stars were selected according to the following properties : having $7.8 < K < 10$ and $(J - K) = 0.64 \pm 0.1$, having known V magnitudes and known proper motions[3]. Moreover, selecting stars with apparent magnitude lower than $K = 10$ puts an upper limit on the distances of the red clump stars of about 2.5 kpc from

[3]The proper motion of a star is its relative displacement over time projected on the sky, as we see it from earth.

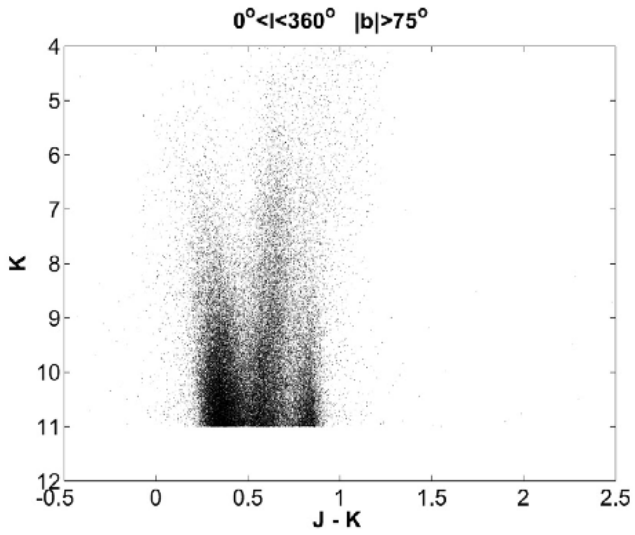

Figure 2.3: NIR colour-magnitude diagram of all the 2MASS (Two Micron All Sky Survey) fields in 15° around the galactic poles. J and K are fluxes from their respective photometric band. Reference: figure 1 from Cabrera-Lavers et al. (2005).

the sun (see Cabrera-Lavers et al., 2005 for details). Therefore, the above points are good selection criteria for targeting red clump stars farther than the solar neighbourhood.

[Fe/H] was expected to cover a range of about 1.25 dex, also, having 5 stars per 0.25 dex is considered reasonable for tracing one trend. As we want to be able to distinguish two trends, considering around 50 stars should suffice. Practically, Daniel Adén and Jennifer Simmerer performed one observing run in 2008 while Thomas Bensby and Daniel Adén performed another one in 2009. Both runs used the Magellan Inamori Kyocera Echelle (MIKE) spectrograph (Bernstein et al., 2003) on the Magellan Clay 6.5 m telescope operating at Las Campanas Observatory in Chile. From these runs, we obtained spectra of 43 red clump stars of high resolution[4] and high signal-to-noise ratio (SNR)[5] in the visible, typically ranging from 4800 Å to 8600 Å in wavelength, and whose stars are located towards the north galactic pole at unknown but estimated distances ranging from 0.5 to 1 kpc.

Finally, the data were reduced in the same way as described in Bensby et al. (2014): using the MIKE IDL pipeline[6] by Burles, Prochaska and Bernstein, and observing for each run rapidly rotating B stars in order to divide out telluric lines and some residuals in the last stages of the data reduction.

2.5 Presentation of our data

The raw data, as "seen" by the CCD camera, are echelle spectra where the orders appear as stripes (practically, the different orders of the light diffracted by the gratings used) of charge

[4]Only the red CCD was used to get the spectra, and the slit width of 0.35" used during the runs gave a resolution power of 65 000.

[5]In average, the spectra have SNR of 160 at 5500 Å and 200 at 6500 Å.

[6]See `http://web.mit.edu/~burles/www/MIKE/`.

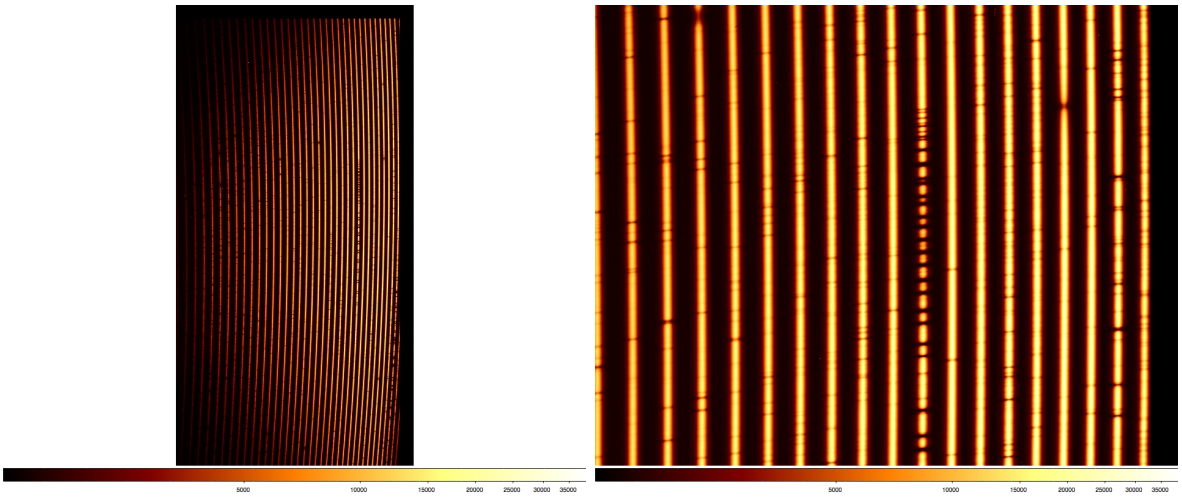

Figure 2.4: Left panel : representation of the raw data of a stellar atmosphere seen by the CCD chip. The colour is in arbitrary intensity unit. Right panel : close-up area of the left panel image where absorption lines are clearly seen.

counts that we can convert to an intensity of arbitrary unit. The stripes evolve according to wavelength. As we can see figure 2.4 left panel, the overall maximum intensity is not the same from one side of the image (actually, the CCD chip) to the other. This effect is a parasite that can be due to the fact that pixels' sensitivity of a CCD chip depends on wavelength. Figure 2.4 right panel shows a close-up area of the raw data where we can clearly see variations of intensity, along the stripes, which are photons more or less absorbed at the corresponding wavelengths: they are the absorption lines in the reduced spectra. The different orders are connected to each other to form a continuous wavelength axis, and the parasites are canceled out, through the reduction process.

Even though our spectra have high resolution and SNR, the data reduction process is not perfect and can create unexploitable areas. Indeed, vertical gaps in the continuum level can occur due to residuals from the reduction: this can be seen in left panel figure 2.5 where the peaks come from the division of highly rotating B star template in order to cut the telluric lines from the earth's atmosphere. But, even if these regions become unexploitable, the reduction force us to avoid these regions which keeps us away from erroneously measuring telluric lines. Nevertheless, cosmic rays can create uneven huge peaks, locally disturbing the spectra.

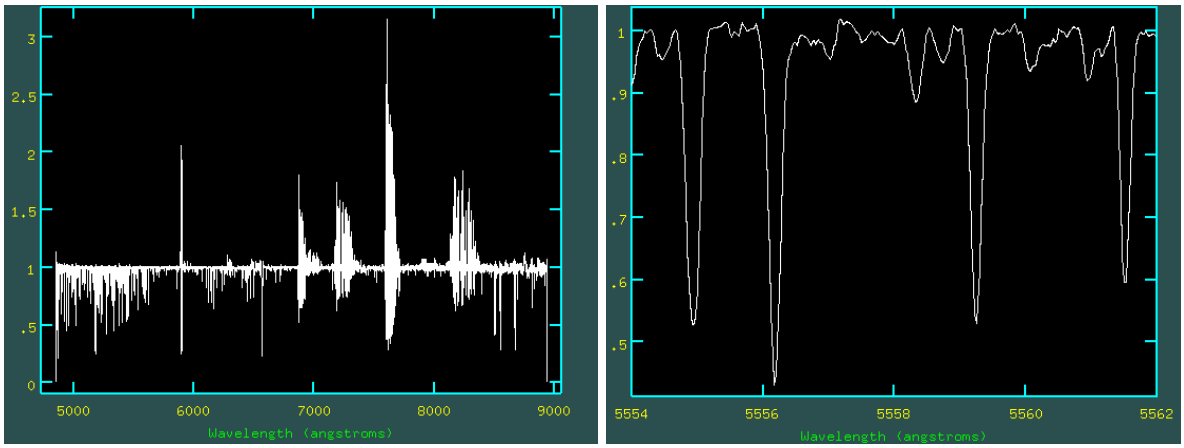

Figure 2.5: Left panel : image of a reduced spectrum through its full range of wavelength. The 5 distinct features along the spectrum that make the concerned areas unexploitable come from the cut of telluric lines. Right panel : close-up on a clean area which shows, among others, the first line of our line list for the element Al, at 5558.32 Å for this spectrum.

Chapter 3

Tools for spectra analyses

For this work, we rely on the spectra of 43 stars expected to be red clump stars located approximately up to 1 kpc above us in the direction of the north galactic pole. Then, tools allowing the determination of relevant stellar parameters from spectral lines are needed in order to infer the chemical and kinematic properties and distributions of these stars. A method often used in the literature to do so is the measurement of equivalent widths of relevant absorption lines following by the fitting of stellar photospheres' models to the values measured. Several softwares have been developed to be partly or totally dedicated to this task. Among them we can find manual (interactive) softwares, semi- and fully-automatic ones.

We considered in this study that for equivalent width measurements fully-automatic softwares were not pertinent to use. Indeed, they work as black boxes where the user cannot see how the measurements are done, and as a consequence, if they are done correctly, while it has to be considered as a serious issue since spectra contain imperfections that only the human eye can detect (a bad reduction of the spectrum or a cosmic ray near a line being measured for instance). On the opposite side, fully-manual tools are really precise to perform equivalent width measurements, but since almost 500 lines have to be measured in each spectrum for this study, this task becomes really monotonous and time consuming. That is why, after having measured some lines in a fully-manual way with the IRAF task 'splot' for comparison purposes, we chose to use TAME which has a semi-automatic option.

3.1 IRAF

IRAF[1] (Image Reduction and Analysis Facility) is a fully-interactive software whose task 'splot' (from the 'noao.onedspec' package) allows the measurement of spectral lines' equivalent widths among other parameters. The IRAF's input is simply the spectrum image in a '.fits' format. The user has to specify manually the window of investigation for each line to measure. Then, one method is to set two points on the continuum level in each side of the line and to specify the line profile to use. Then, IRAF computes the equivalent width of the line between the two points from the profile chosen (gaussian in our case, but lorentzian or voigt can be used instead), see figure 3.1. Then, its graphic interface print the parameters computed (the centre of the line, its flux, the EW, and the FWHM (full width at half maximum) of the profile used) which are also saved in a log file.

[1]Developed at the National Optical Astronomy Observatory, see `http://iraf.noao.edu` for details.

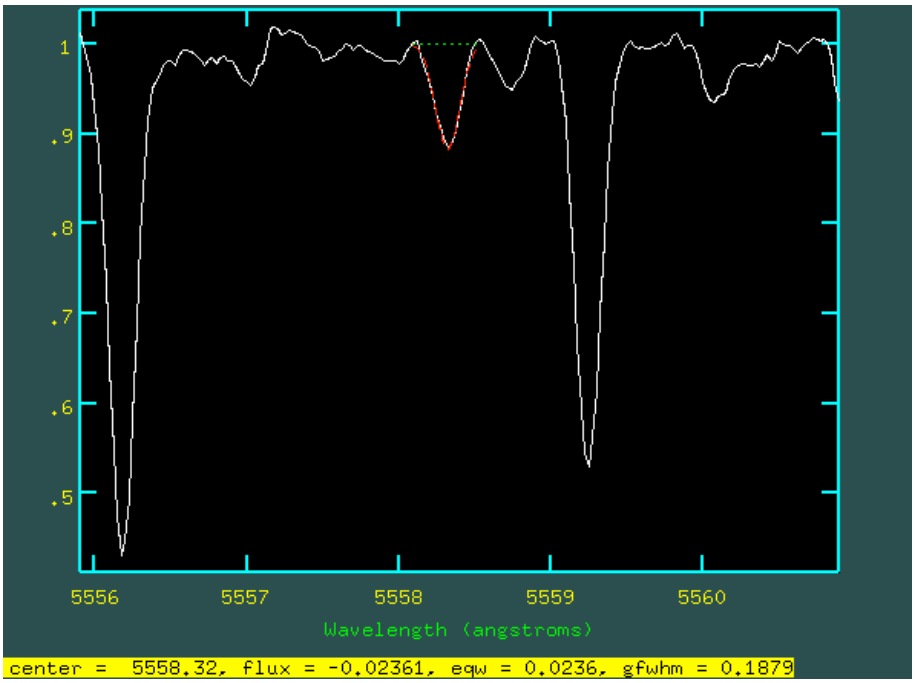

Figure 3.1: Fitting of a gaussian profile (the red dashed line) to a line produced by the element Al using IRAF (it is the same line as in the right panel of figure 2.5). The fitted continuum level is indicated by the green dashed line. The parameters are highlighted in yellow, with the EW in Å here.

So, the user has a full control on what is being measured, which makes IRAF a secure way to get precise measurements. However, measuring each line by hand by specifying the window range and by setting points around the line is a tedious task since the number of lines used is 496 in this study, and so for each spectrum.

3.2 TAME

TAME (Tool for Automatic Measurement of Equivalent width), presented by Kang & Lee (2012), is a software running under IDL which allows the measurement of the EWs of spectral lines either automatically or interactively (semi-automatically). In its semi-automatic mode, TAME fits, line by line (according to a line list provided by the user), the continuum and the line considered in the current window and allow the user to make some changes at each step. Indeed, before to switch to the next line, the user can see the result of the fitting and the corresponding values (EW, λ of the line's peak, χ^2 of the fitting, radial velocity shift, FWHM, ...), and, according to what has been done by the software, the user can perform several actions including to change the profile (between gaussian and voigt), to move the continuum up or down, set his own continuum points, delete some points of the spectrum, move the spectrum in wavelength if the wrong line is being measured, or skip the line if nothing can allow a good measurement. In that way, TAME is an improvement compared to IRAF since the user can actually choose not to save the experiments in the current working window and skip a line if need be whereas IRAF constantly save every test. Also, as the fitting is first done automatically as well as the next line is automatically reached after the user decides to

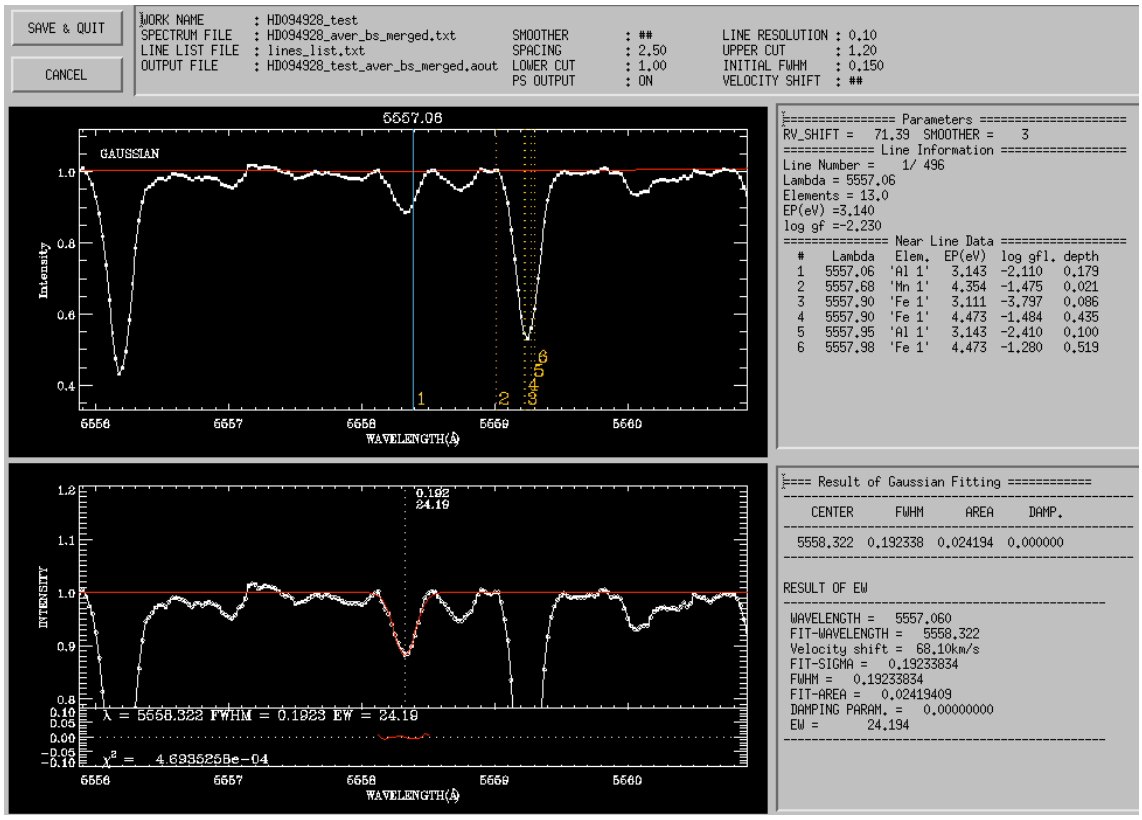

Figure 3.2: Fitting of a gaussian profile (the red line) to the same line as in figure 3.1 page 14. The top panel is the interface where the user can work (set points, move the continuum...), the bottom panel is the result of the fitting. The EW is in mÅ here.

save or not the parameters, a precious amount of time is saved compared to IRAF and the user can actually focus on the measurements. Much more parameters than with IRAF are shown to the user, see figure 3.2.

3.3 AMOOG

MOOG[2] is not properly speaking a software of spectra analyses, but is a bridge which takes as input the TAME's (or IRAF's) output and gives as output relevant atmospheric parameters and the abundances of the stars. The relevant atmospheric parameters are : the effective temperature T_{eff}, the surface gravity $\log g$, the metallicity [Fe/H] and the micro-turbulence velocity V_t of the stars. The elements for which MOOG returns an abundance are the ones for which at least one spectral line had been measured with TAME (or IRAF). The stellar parameters and abundances, correlated, are computed iteratively. In fact, we used in the study AMOOG which is a wrapper written in R by Gregory Ruchti that runs MOOG in an automatic way until input and output stellar parameters converge. In order to compute the stellar parameters and abundances, MOOG is also based on the individual equivalent widths

[2]See `http://www.as.utexas.edu/~chris/moog.html` for details.

as well as the excitation potentials, the reduced equivalent widths, and the wavelengths of the lines measured. This computation is based on basic equations that govern the stellar photospheres under usual simplifications assuming: a thermodynamical equilibrium state in each volume considered during the computation (called LTE for local thermodynamical equilibrium), a plane parallel geometry ("making all physical variables a function of only one space coordinate", Gray, 2008, p.172), a hydrostatic equilibrium (no large-scale accelerations in the photospheres), and excluding magnetic fields.[3]

[3]These assumptions are denoted hereinafter 1-D LTE.

Chapter 4

Abundances

The chapter aims at determining the stellar parameters and abundances of each star in our sample. Indeed, since red clump star photospheres are preserved, the abundances of the stars lead to the abundances of the gas clouds they formed from: differences in the stars' abundances will therefore highlight differences in the chemical composition of their natal regions.

To do so, we first measure the strengths of observed spectral lines of the stars, which are representative of the proportions of chemical compounds in their photospheres. From these measurements and consistency checks, we are able to compute the atmospheric parameters and abundances using model photospheres. Then, the atmospheric parameters help us to verify the red giant nature of our stars, and, finally, the abundances of the elements can be analysed and compared to other studies.

4.1 Determining the stellar abundances

4.1.1 Measuring the equivalent widths of the stars with TAME

The strength of absorption lines is proportional to the presence of chemical elements in the stellar photosphere. A way to measure the strength is to measure the EWs of the spectral lines. Indeed, the equivalent width is, practically, the width of a rectangle of height the height of the local continuum and of area the one of the spectral line (measured by a numerical fitting), see figure 4.1. Therefore, its value does not depend on the shape of the lines (which can vary because of doppler shift for instance), hence yield the right number of absorbed photons. Even if interstellar dust diminish the total amount of light received, the equivalent width is not affected since the continuum is normalised to 1 and the equivalent width "measures the fraction of energy removed from the spectrum by the line" (Spitzer, 1978).

Equivalent widths have been measured using TAME's automatic fitting of gaussian profiles to the absorption lines' shapes. The continuum level was for each line visually checked and, in case of a bad alignment with the real continuum of the local area around a measured line, moved up or down or manually set (by setting by hand several points by which the continuum must pass). For self-consistency purposes, we stuck to gaussian lines for all lines, and simply skipped the lines where a voigt profile was more appropriate or where none gave consistent fittings.

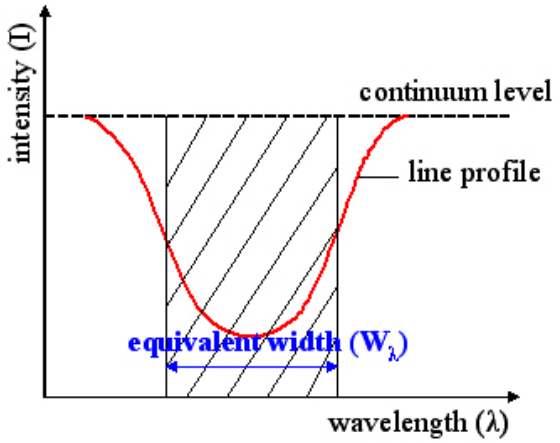

Figure 4.1: This diagram is a representation of an equivalent width, with given line profile and continuum level. Figure reference : `http://en.wikipedia.org/wiki/Equivalent_width`.

4.1.2 Getting the abundances and atmospheric parameters with AMOOG

Measuring lines in stars' spectra appears to be relevant since line strength can be expected to increase with an increase in the chemical abundance of a given absorber compound in a star's photosphere. But the relation between line strength and elemental abundance is not a simple proportionality and depends on the optical depth in the line. Indeed, for weak lines the depth grows in proportion to the abundance: the equivalent width of such a line is proportional to the abundance. But, for stronger lines there is a saturation effect, hence the equivalent withs of strong lines are approximately proportional to the square root of the abundance (Gray, 2008, p.326-327). Also, strong lines are expected to show deviations from the local thermodynamic equilibrium (LTE) because of damping effects (roughly speaking Van der Waals interactions) resulting in an enlargement of the lines' wings. A non-LTE approximation would thus be required for the determination of the abundances of compounds producing strong lines. The nice solution that AMOOG uses to bypass this issue is in fact to only keep the equivalent widths of, accurately measured, weak and normal lines in order to fit them to the model atmosphere under LTE approximation. Hopefully the number of weak and normal lines is high enough to get reliable stellar parameters and abundances, but we still have to keep in mind that sometimes small deviations can be seen because of this effect. In that way, we ran AMOOG under an LTE model atmosphere as first approximation.

Practically, the code is an iterative process starting with initial atmospheric parameters and evolving to reach three equilibria that set the final parameters setting the final model photosphere which then computes the elemental abundances considering the equivalent width measurements. To obtain the parameters, $T_{\rm eff}$, $\log g$, [Fe/H] and $V_{\rm t}$ and mean α-element abundance are modified at each step and re-derived until the conditions of equilibria are reached. The MOOG code, summarised in Magrini et al. (2013), works as follow:

Physical determination of [Fe/H] and the other elements

Based on initial values of the stellar atmospheric parameters set by the user, a first Kurucz[1] 1-D LTE model atmosphere is computed. Using the equivalent widths measured, the fitting of the model to the measurements set a first estimation of the iron abundances which are used to compute T_{eff}, $\log g$ and V_t. The new values are then used to compute a new model atmosphere. This process iterates until a convergence is reached. The convergence set the final Kurucz model atmosphere from which the abundances are computed by fitting of the curves of growth to the equivalent widths measured.

Physical determination of T_{eff}

The determination of T_{eff} uses the principle of excitation balance of FeI lines. FeI abundance is linked to effective temperature and to the excitation potential of FeI lines having equal energy level (see equation 1 in Magrini et al., 2013). Therefore, T_{eff} is found when the mean FeI abundance calculated for each level of excitation potential is the same from one level to another. We can note that a direct consequence is that T_{eff} is better estimated when the lines used cover a wider range of excitation potentials. In that way, the more we have lines effectively measured, the more T_{eff} is likely to be better estimated.

Physical determination of $\log g$

The determination of $\log g$ is based on the ionisation balance between FeI and FeII lines. The abundance of FeII is linked to surface gravity $\log g$ and depends also on the most represented state of the atoms in the photospheres (ionised or neutral; see equation 2 in Magrini et al., 2013). So, as we assume ionisation equilibrium in the stellar photospheres, $\log g$ is found by equalling the FeII abundance to the FeI abundance found from the step of T_{eff} determination.

Physical determination of V_t

The determination of V_t works on the balance of FeI abundance with reduced line strength. The microturbulence is a representation of particular motions in the stellar photospheres contained in small volumes, typically smaller than the mean free path of the photons (Bensby et al., 2003). These motions perturb the shapes of the lines and are correlated to their strength: stronger lines are more affected than weak lines (which is another reason why strong lines are rejected). So, in order to get an estimate of V_t, the different FeI abundances calculated from each line are forced to give a constant abundance with reduced line strengths (measured by the reduced EW defined by $\log(EWs/\lambda)$).

We have to note that the previous explanations describe the main processes affecting the determination of the atmospheric parameters. But a change in one parameter affects also the others: the parameters are correlated and are therefore computed all at the same time iteratively.

[1] See `http://kurucz.harvard.edu`

4.1.3 Improving the results

Because of the high number of absorption lines considered for each spectrum and the fact that the shapes and strengths of the lines differ from one spectrum to another, it is for most of the lines visually impossible to know if it is actually the good one which is being measured by TAME. Though, the value of the velocity shift helps a lot to counter-balance this bad point since it should not really differ from one line to another inside the same spectrum. Therefore, constantly checking the velocity shift for each line when measuring them with TAME semi-automatic mode is good guarantee of actually fitting the right line. However, when lines are blended or really closed, it is not unlikely that TAME can fit the wrong line, leading to a wrong equivalent width value, especially when a strong line is near a small true one.

Therefore, it is really important to check back how scattered are the points of each elements around their mean abundance, and for those which are outlying, manually check their EW value with IRAF and remove them from AMOOG input file accordingly[2]: if IRAF and TAME values are consistent there is no reason to remove a given line[3], but if it appears that the wrong line has been measured or if the EW values don't agree then there is no reason to keep this line in AMOOG input file.

After having being careful about the velocity shift, having a good continuum level and a good line fitting while measuring the stars' absorption lines with TAME interactive mode, all the iron I and iron II outliers, typically showing a deviation from their mean value greater than $\pm 2\sigma$ (that is to say approximately ± 0.3 dex or more), from AMOOG output file have been checked back and removed if need be in order to improve the stellar parameters' and abundances' results.

As expected it appeared that the outliers were mainly produced by the same lines from one spectrum to another (see figure 4.2) which were, for several, small lines really close to a strong one or really small lines almost lost in the continuum near stronger ones; TAME expectingly measuring the stronger ones instead of the true ones in these cases.

Therefore, re-running AMOOG without considering bad measurements changed the atmospheric parameters' values consistently with the recurrence of the same bad measured lines through the different spectra while improving their reliability. The top panels and bottom left panel figure 4.3, show the consistent change in the results, where $T_{\rm eff}$, $\log g$ and $V_{\rm t}$ are lower for all the stars, of 48 K (standard deviation of 32 K), 0.05 dex (± 0.08 dex) and 0.08 km/s (± 0.08 km/s) respectively. However, the metallicity and overall abundances were not really affected by such an improvement, which confirms that they are reliable and that the spectroscopic method is robust (see the bottom right panel of figure 4.3).

[2]Indeed, even if this step can be kind of tedious, it is really important because "blindly" removing lines higher than a given value over or under the mean abundance is not meaningful since the scatter in abundances depends strongly on the quality of the spectrum which varies from one to another. Thus, it is much more coherent to analyse in the spectra if there are recurrent lines that have the highest scatters.

[3]Indeed, as we cannot determine the origin of such an outlier (: unexpected but still real feature of the star or introduced by any other mean?) it is much more consistent to keep this line and have a higher uncertainty in the determination of the abundances rather than narrowing the uncertainty around another mean abundance by removing the given line without knowing the reason why it is an outlier.

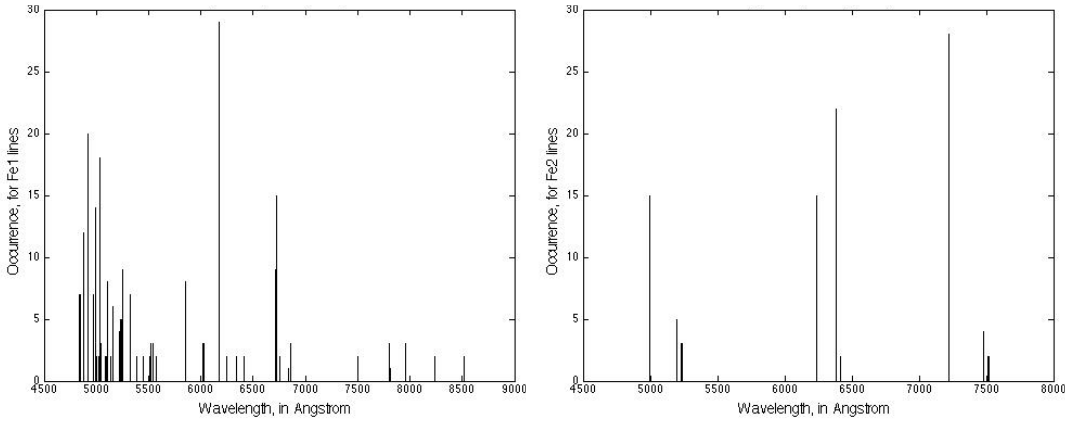

Figure 4.2: Distribution of the FeI (left panel) and FeII (right panel) lines removed from AMOOG input file for having being inconsistently measured with TAME. The distribution shows that it was mainly the same lines which where causing troubles from one spectrum to another.

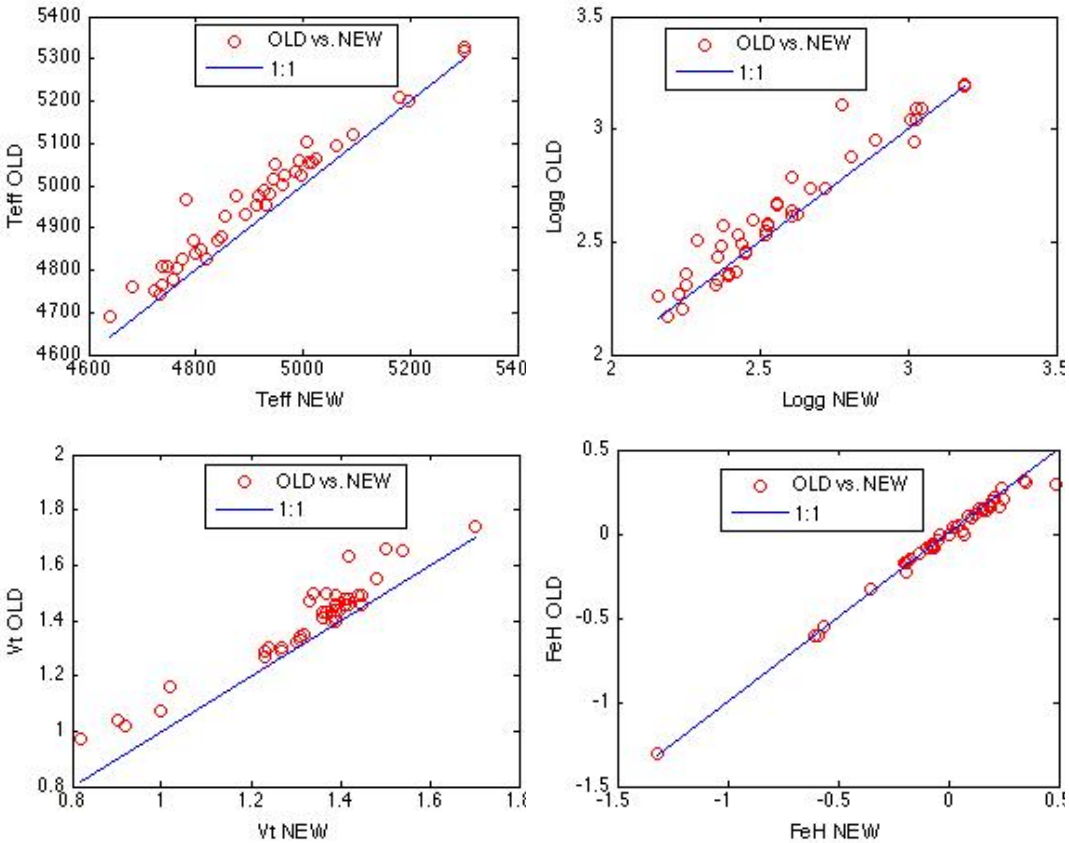

Figure 4.3: This figure shows the changes in $T_{\rm eff}$ (top left panel), $\log g$ (top right panel), $V_{\rm t}$ (bottom left panel), and [Fe/H] (bottom right panel) before and after having conscientiously removed the FeI and FeII outliers of our first results from AMOOG input file. Improved values are lower for $T_{\rm eff}$, $\log g$, and $V_{\rm t}$; no trend in change is shown for [Fe/H].

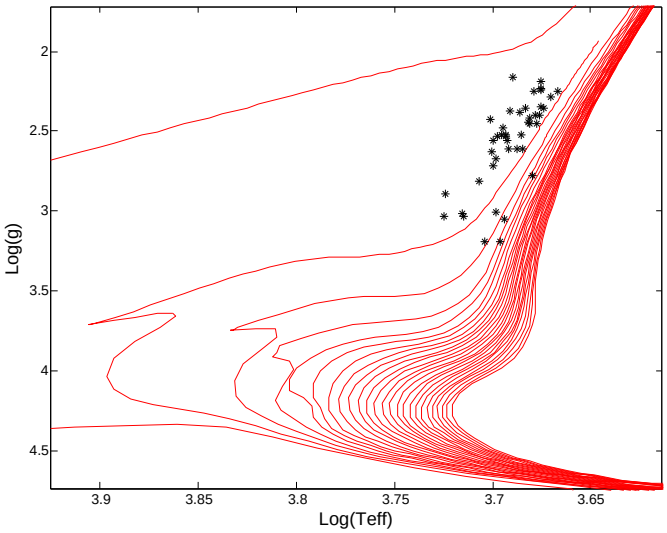

Figure 4.4: HR diagram of our red clump stars, along with the isochrones [Fe/H] = −0.3 dex. Isochrones of higher or lower metallicity would mostly shift along the x-axis compared to the y-axis. Our stars follow the giants' tracks as expected. Ages cannot be determined. From left to right the isochrones correspond to evolutionary tracks for ages 0.1 Gyr, and then 1 to 24 Gyrs by steps of 1 Gyr.

4.1.4 HR diagram of our red clump stars

From the stellar parameters calculated in the previous step, we can plot an HR diagram of our stars along with isochrones in order to visually confirm that our stars are clumped as expected above the main-sequence following the red giants' tracks. From the parameters calculated, we draw in fact a 'modified' HR diagram which relies on $\log(T_{\rm eff})$ in x-axis and $\log g$ in y-axis (both increasing towards their crossing point). Figure 4.4 shows that our stars are, as expected, located above the turn-off point and that they follow the tracks of the red giants. We used the Yonsei-Yale improved isochrones (Demarque et al., 2004) for a metallicity of [Fe/H] = −0.3 dex. Ages of the stars cannot be inferred from the isochrones since isochrones mostly shift in $\log(T_{\rm eff})$ according to metallicity (which varies from one star to another) and evolutionary tracks are too closed to each other in this area.

4.1.5 Stellar abundances

Normalisation of our data

We obtained in the above steps the abundances of 16 elements for each star. AMOOG automatically gives these abundances relatively to the abundance in hydrogen, calculated from the model (it has to be noted that no hydrogen lines have been measured in the spectra).

In order to be able to do comparisons between the different elements and with other studies, we have to think of a way to normalise our data. The usual way is to normalise them to solar values. However, even if the sun has been subject to many and deep investigations, the solar abundances slightly varies from one study to another (see Grevesse & Sauval (1998) and Asplund et al. (2009) for instance). Moreover, the method used in those studies to determine the stellar abundances can differ from the method we used here. Therefore, we chose to determine our own stellar abundances in order to be self-consistent.

The solar spectrum we used has been obtained in 2006 with the MIKE spectrograph by looking at the reflection of the solar light on Saturn's moon Ganymede. Thus, we have for our solar spectrum the same resolution as for the spectra of the red clump stars. As for the SNR, its value is about 250 at 5500 Å and 300 at 6500 Å. The method of abundance determination performed is the same as before. The abundances obtained are globally in better agreement with Grevesse & Sauval (1998) than with Asplund et al. (2009), but in both cases our solar abundances are in average higher than theirs of approximately 0.1 dex; the reason is unclear and it is beyond the scope of the current study to delve deeper into. Therefore, we keep our solar abundances for the normalisation.

Hence, the hereinafter abundances noted [X/H] are normalised abundances, so that: $[X/H] = \log\left(\frac{N_X}{N_H}\right)_\star - \log\left(\frac{N_X}{N_H}\right)_\odot$.

Relevant abundance plots

After the normalisation of the data, we can plot the abundances of our sample of stars. The abundances [X/Fe] are plotted against metallicity [Fe/H]. Figure 4.5 shows the plots of all the elements from which lines have been measured, that is to say: AlI, BaII, CaI, CrI, CrII, FeI, FeII, MgI, NaI, NiI, OI, SiI, TiI, TiII, YII, and ZnI. The more we have measured lines for one element, the more we can supposedly trust the mean abundance value of this element. From the lines' list we used, and accounting for skipped lines directly when using TAME, or for conscientiously removed outliers in the case of FeI and FeII, we measured in average 209 lines for FeI, 52 for NiI, 30 for SiI, 23 for FeII, 21 for TiI, 19 for CaI, 12 for TiII, 11 for CrI, 7 for YII, 6 for AlI, CrII, and OI, 5 for MgI, 4 for NaI, 3 for BaII, and 1 for ZnI. The error bars in the abundance plots are therefore representative of these numbers: we have computed the formal error (line-to-line scatter divided by the square root of the number of lines) for each star and each element, and indicated a typical value on the plots. However, as we have only one line for ZnI, the uncertainty in [Zn/Fe] shown is only due to the propagation from the uncertainty in metallicity. Values of the abundances, their uncertainties, and the atmospheric parameters are gathered tables A.1, A.2, and A.3.

4.2 Inferring stellar chemical properties

4.2.1 Comparison to Mishenina et al. (2006)

In their paper, Mishenina et al. (2006) determined the atmospheric parameters of 177 red clump stars of the galactic disc (also called clump giants) and their abundances for the elements Li, C, N, O, Na, Mg, Si, Ca and Ni.

Their sodium abundance ([Na/Fe] vs. [Fe/H]) resembles ours (panel (1,3) figure 4.5), with stars showing no trend and being spread in the box [-0.8, 0.3] in [Fe/H] and [-0.1, 0.4] in [Na/Fe]. We note that they have around 20 stars with [Na/Fe] under 0 dex while we have only one in our sample (in the mentioned box), but this can be either due to our less numerous sample, or to a shift coming from different solar values used for our respective normalisations.

For [O/Fe] vs. [Fe/H] (panel (3,3)), the trend is similar, showing a thick slope starting at -0.2 dex in [O/Fe] for the more metallic stars and reaching 0.6 dex for the poorer metallic ones. Here again we have proportionally less stars whose abundance is under solar.

For Mg (panel (2,3)), the same trend is shown. Both studies (theirs and ours) show a slope of increasing Mg enhancement with decreasing metallicity. This slope is thinner and

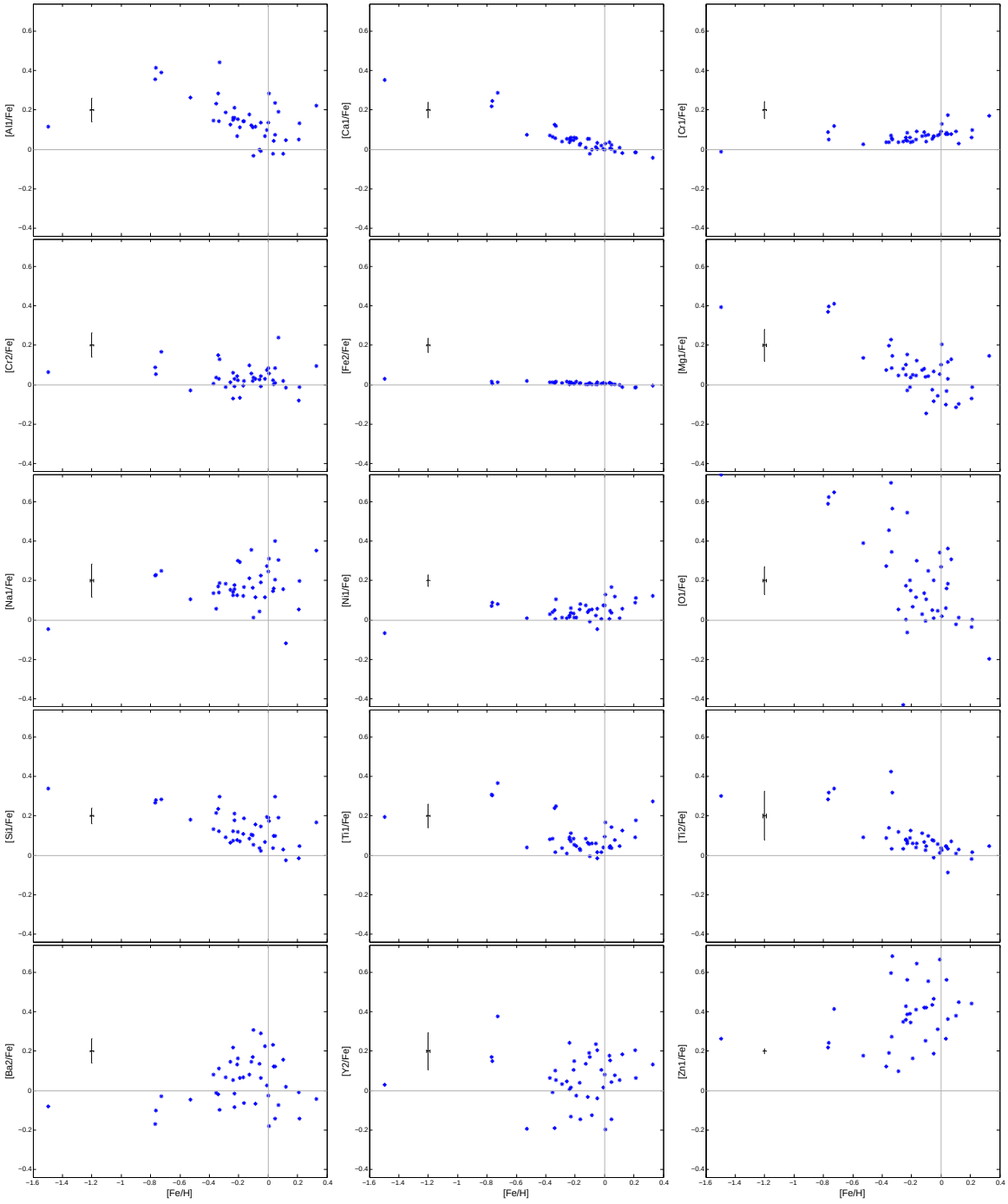

Figure 4.5: From top left to bottom right, abundances of the elements: AlI, CaI, CrI (first row), CrII, FeII, MgI (second row), NaI, NiI, OI (third row), SiI, TiI, TiII (fourth row), and BaII, YII, ZnI (fifth row) with respect to Fe, versus [Fe/H], all normalised to the sun. Typical formal errors are also shown. Panel (2,2) shows [FeII/Fe] vs. [Fe/H] and reveals a near perfect flat trend as expected in the assumption of ionisation balance.

more moderate than for oxygen, reaching 0.4 dex in [Mg/Fe] for the metal poor stars. Here, we also have under solar abundances for the more metallic stars, however it seems that their under solar [Mg/Fe] stars are more numerous than for [Na/Fe] and [O/Fe].

Si (panel (1,4)), another α-element along with Ca, Mg, O and Ti, shows a similar behaviour. Indeed, all stars have over solar [Si/Fe] abundance, and are confined between 0 and 0.3 dex, and tend to show a moderate slope from (0,0) to (-0.8,0.3) ([Fe/H], [Si/Fe]).

For Ca (panel (2,1)), the trend is the same: a moderate slope starting below near solar values for the more metallic stars and reaching around 0.2 dex for the metal poor stars (disregarding our lowest metal poor star); however our stars show much less scatter in abundance hence the trend is really well defined in our case.

As for [Ni/Fe] vs. [Fe/H] (panel (2,3)), the abundance trend is the same except that our Ni abundances are slightly above theirs. We see in both plots a constant near solar Ni abundance for stars with [Fe/H] < 0 dex, while stars with [Fe/H] > 0 dex show a slight Ni enhancement.

Mishenina et al. (2006) also reported that the α-element abundances as well as the Ni abundance (iron-peak element) of red clump stars behaved as dwarf stars, allowing us to use them to study the chemical and dynamical evolution of the galaxy.

4.2.2 Comparison to Bensby et al. (2014)

Bensby et al. (2014) determined atmospheric parameters, stellar ages, kinematics, orbital parameters, and abundances of 13 elements (O, Na, Mg, Al, Si, Ca, Ti, Cr, Fe, Ni, Zn, Y and Ba) for 714 F and G dwarf stars located in the solar neighbourhood. Globally their sample has a wider range in metallicity with $-2.8 <$ [Fe/H] < 0.5. However, inside the range of our sample, the trends are globally the same.

The oxygen abundance shows again the steeper slope reaching above 0.6 dex in [O/Fe] for stars whose metallicity is around -0.4 dex or below. The abundance of stars with metallicity below -0.8 dex flatten confirming a coherent behaviour for our most metal poor star.

[Mg/Fe] vs. [Fe/H] shows a matching behaviour: stars appear to be more and more Mg-enhanced as metallicity decreases until -0.8 dex in [Fe/H] from where a flat Mg-enhanced trend at poor metallicity is seen in their sample and confirmed in ours by our metal poor star having [Fe/H] < -1.4 dex.

For Al (panel (1,1)) the similarities are less clear even though they reported Al to behave as an α-element regarding [Fe/H]. In our case, the trend in Al abundance is clearly characteristic of an α-element: slope of increasing Al abundance with decreasing metallicity, starting around solar values.

The Si abundance seems in better agreement here, since the abundances are again mostly over solar abundance and, moreover, the trend characteristic of the α-elements is clear in Bensby et al. (2014) while it was fuzzy in Mishenina et al. (2006). The flattening enhanced part at low metallicity is also in agreement.

Ca shows also the clearer behaviour in their study, with a slope showing really little scatter and abundances starting to flatten around 0.2 dex in [Ca/Fe] below -0.8 dex in metallicity.

As for Ti, our values are in better agreement when considering TiII (panel (3,4)) instead of TiI (panel (2,4)). Indeed, our TiI abundances show an increase for stars over solar metallicities, which does not appear for our TiII abundances and which is not clearly seen in their study. This effect can be due to non-LTE effects that affect TiI lines (Bensby et al., 2003).

However, the trend for under solar metallicity abundances are in agreement (still better for TiII) since abundances are confined in the same ranges of [Ti/Fe] and show all the previously mentioned characteristics of the α-elements.

Na, Cr and Ni are confined near solar abundances whatever the metallicity is, and never exceed a scatter of ± 0.2 dex; which is what is seen in our plots except that our CrI (panel (1,3)) and our Na abundances are slightly over theirs. The ionised compound (CrII, panel (2,1)) is here again in better agreement than the neutral one.

BaII (panel (1,5)) shows a similar behaviour with an enhanced peak slightly below solar metallicity, while poorer metal stars have a slightly below solar abundance. YII (panel (2,5)) is confined in the same ± 0.2 dex around solar abundance but the trend is clear in their study while it is fuzzy in ours. Finally, our Zn abundance is enhanced by approximately 0.2 dex and is fuzzy while theirs show a similar behaviour as YII; but we must highlight that only one line has been measured for Zn in our study, which is not satisfactory.

Our red clump abundances are globally in agreement with abundances of dwarf stars, and, notably, the α-elements show the same characteristic trends: enhancement with decreasing metallicity until a flat α-enhanced trend at poor metallicity. Therefore, as mentioned in Mishenina et al. (2006), we can coherently use red clump stars to perform a chemical and dynamical study probing the evolution of the galaxy.

4.3 Conclusions

The aim of this chapter was to determine the atmospheric parameters and abundances of our red clump stars. To do so, we first measured the equivalent widths of nearly 500 lines for each star spectrum, using the semi-automatic mode of TAME. Then, with our measurements as an input, we computed a first set of atmospheric parameters and abundances using AMOOG, which is based on Kurucz model photospheres under 1-D LTE assumption. The line-to-line scatter in FeI and FeII abundances (used by AMOOG to compute the final model atmosphere) showing an enhanced scatter due to repetitive outliers, we then checked their consistency by comparing TAME and IRAF values. We removed, from our equivalent width measurements, outliers for which we found a rational explanation explaining why they were erroneously outlying, and ran again AMOOG with our more coherent set of measurement and obtained our final stellar parameters and abundances that we normalised to our own solar abundances measured consistently. We checked that our stars were located on the giant branch of the HR diagram as expected; and abundance uncertainties were calculated based on the line-to-line scatter and the number of lines used.

This enabled us to infer purely chemical properties for our red clump stars: we plotted the abundances [X/Fe] vs. [Fe/H] for all the elements and found behavioural consistency with other red clump and dwarf star abundance studies. Particularly interesting is the common trend among the α-elements (Ca, Mg, O, Si and Ti, and Al which behaves equally) showing a slope, starting near solar values, where abundance increases with decreasing metallicity before to flatten at poor metallicity; typically below -0.6 dex. We can highlight that 4 of our stars, having low metallicity (below -0.6 dex) and the highest α-enhancement among our sample, have high likelihood to belong to a thick disc population since several studies reported a metal poor α-enhanced thick disc, while thin disc stars have near solar values in these studies.

Chapter 5

Kinematics

This chapter aims at determining the kinematics of each star in our sample. Indeed, even though we see different abundance proportions inside our sample, the abundances only do not provide enough information to distinguish between different populations. Moreover, studies using data from the solar neighbourhood showed that thin and thick disc stars have different abundances and kinematics. Therefore, determining the kinematics of the stars seems legitimate in order to discern the populations, if discernible.

To do so, we first gather useful parameters already available in the literature or determined during the abundance study in order to compute the distances of our stars. These parameters are: coordinates, fluxes, proper motions, radial velocities, and metallicities. The distribution of dust inside the Galactic disc is taken into account as it would impede the determination of the distances otherwise. Once the distances are known, we compute the space velocities of the stars also using the previous parameters: coordinates, proper motions and radial velocities particularly. From positions and space velocities we then compute orbital parameters of the stars, particularly useful for the coming investigations. Finally, we verify that the targeted stars are actually outside the solar neighbourhood, and analyse the repartitions of positions and space velocities among the stars.

5.1 Determining the stars' kinematics

5.1.1 The SIMBAD database

We made use of the SIMBAD database operated at CDS, Strasbourg, France[1] to gather useful properties of our stars that are already available in the literature. We gathered stars' coordinates, magnitudes (B and V), proper motions, and radial velocities (note that radial velocities were not available for all stars). The references used for each property and each star are gathered in table B.1. Hereinafter, "literature" means from the papers listed in the table.

5.1.2 Radial velocity correction

The radial velocities (RVs) given by TAME, based on the lines' shifts of the spectra, can not be taken directly since it does not take the barycentric shift into account. Indeed, the MIKE

[1] `http://simbad.u-strasbg.fr/simbad/`

spectrograph, being on Earth, has a proper shift due to the Earth rotation around the sun and around its own axis. Thus, a barycentric correction has to be applied to TAME values. But, this step is not enough to obtain the real RVs of our stars as the reduction process of the spectra led to an additional offset in the spectra shifts, whose source being unfortunately unknown.

Fourteen of our 43 stars had previously recorded RVs in the literature. Using these values, this offset has been calculated back, from the true measured RV values, the TAME values, and the barycentric correction of these 14 stars. The offset, nearly the same among the 14 stars with a mean of 82.86 km/s and a standard deviation of 0.84 km/s, is then subtracted from the TAME RVs after barycentric correction, leading to the final measured RVs of our 43 red clump stars.

5.1.3 Getting the stars' distances

Red clump stars are confined in a small range of colour and magnitude making them good distance indicators: they have been used to measure distances to the galactic center (Paczyński & Stanek, 1998), to the galaxy M31 (Stanek & Garnavich, 1998), or to stellar clusters and other nearby galaxies for which red clump stars are resolved (Pietrzyński et al., 2003). Indeed, their absolute magnitude (a measure of the brightness of a star observed on earth as if the star was at a distance of 10 parsec) is approximately independent from their mass or age. Instead, their absolute magnitude can be calibrated to their colour and metallicity which are both known (colour from the literature and metallicity from this study). Knowing the apparent magnitude of the stars (their true brightness) one could then calculate their distance since the link between distance and decrease in brightness is an inverse square law (three times farther is equivalent to nine times less bright for instance). However, the interstellar medium is filled with dust which diminishes the amount of light received on earth from the stars. Therefore, we need to apply a correction (called dereddening) to the stars' colours in order to get their apparent magnitude. However, this dereddening factor depends on the stars' distances since the more distant a star, the more its light travels through dust. The only solution to obtain our stars' distances is to compute iteratively[2] the reddening and the distance modulus (which depend on each other) until the difference in distance between a given iteration and the previous one is less than a chosen percentage.

Coordinates and fluxes

Galactic coordinates and fluxes (colours) of all our stars come from the literature. We chose for the stars' coordinates galactic coordinates in degrees at epoch J2000, which are required for the dereddening calculation. B (Blue) and V (Visual) magnitudes are 'uncorrected' apparent magnitudes. Typically, we have $0.790 < B - V < 1.270$ mag with a typical uncertainty of ± 0.053. The map of the coordinates of our stars is also shown figure 5.1.

Dereddening

An initial colour excess $\mathrm{E}(B - V)$ is calculated using the dust maps of Schlegel et al. (1998), which give the total reddening, considering all the dust in a specific line of sight. We then

[2]The script for the distances, and their uncertainties, has been written in R based on two functions provided by Gregory Ruchti.

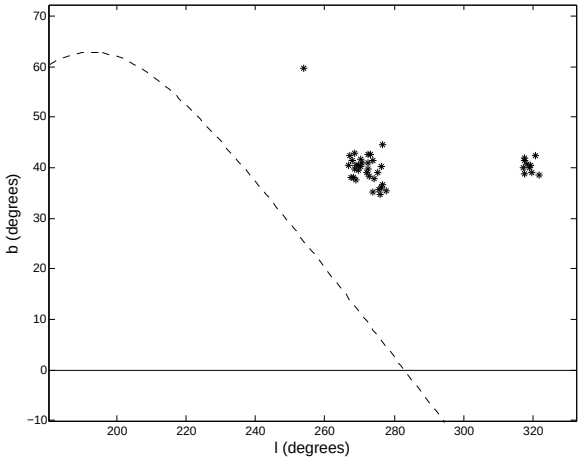

Figure 5.1: Positions of our stars in galactic coordinates (longitude l, and latitude b, in degrees). The solid line at $b = 0°$ represents the galactic plane, while the curved dashed line represents the celestial equator in galactic coordinates, at epoch J2000.

took into account the correction of Bonifacio et al. (2000) who found that the reddening from the Schlegel maps was overestimated for $\mathrm{E}(B-V)_{\mathrm{Sch}} > 0.10$, which is the case for 2 of our 43 red clump stars. The correction is the following:

$$\mathrm{E}(B-V)_{\mathrm{Bon}} = \begin{cases} 0.10 + 0.65 \cdot [\mathrm{E}(B-V)_{\mathrm{Sch}} - 0.10] & \text{if } \mathrm{E}(B-V)_{\mathrm{Sch}} > 0.10 \\ \mathrm{E}(B-V)_{\mathrm{Sch}} & \text{otherwise.} \end{cases} \tag{5.1}$$

After the initialisation of the colour excess, a first distance can be estimated which serves for a more accurate calculation (in fact, reduction) of the reddening[3]. In order to do this reduction, we used the exponential model of the dust absorption presented in Bonifacio et al. (2000) where the reduced reddening is $[1 - \exp(-\left|\mathrm{d} \cdot \sin(b)\right| / \mathrm{h})]$ times the total reddening, where d is a star's distance, b its galactic latitude (see figure 5.3), and h the height scale of the dust's model supposed to be 125 parsecs.

This provides a new, more accurate reddening, which, once $\mathrm{E}(B-V)$ have been subtracted from the stars' colours $B-V$ (to get $(B-V)_0$), and A_V subtracted from their visual fluxes V (to get V_0), allows to get a new, more accurate, estimation of the stars' distances we then iterated until convergence of the distances. Typically, we obtained a magnitude correction A_V of 0.167 ± 0.004 mag.

Absolute magnitude

To compute the absolute magnitude of our stars, we use the calibration formula for red clump stars given in Bilir et al. (2013), which is reproduced here:

$$\mathrm{M}_V = 0.627(\pm 0.104) \cdot (B-V)_0 + 0.046(\pm 0.043) \cdot [\mathrm{Fe/H}] + 0.262(\pm 0.111) \tag{5.2}$$

[3]In practice, it is the total absorption in the V band A_V which is subtracted from the visual flux, where $\mathrm{A}_V = 3.07(\pm 0.05) \cdot \mathrm{E}(B-V)$ (McCall, 2004). And the colour excess $\mathrm{E}(B-V)$ is subtracted from the star's colour $B-V$ whose new value serves for the absolute magnitude calculation (see next).

where $(B-V)_0$ results from the dereddening (exactly the colour excess correction), and [Fe/H] is the iron abundance of our stars[4].

Even though the formula is valid for a wide range of $(B-V)_0$ colour and [Fe/H] metallicity: for $0.42 < (B-V)_0 < 1.20$ mag, and $-1.55 <$ [Fe/H] < 0.40 dex, we have to be aware that their formula has been tested only for distances up to 500 pc. The goodness of their formula is unknown for larger distances.

Distance modulus

The distance modulus is:

$$\mathrm{d} = 10 \cdot 10^{0.2 \cdot (V_0 - \mathrm{M}_V)} \tag{5.3}$$

where V_0 results from the dereddening (exactly the V band absorption correction), and M_V from the previous absolute magnitude calculation, and d is the distance of the star from the sun whose 'dereddened' apparent magnitude and absolute magnitude are V_0 and M_V, respectively.

The new distances are then plugged into the dereddening calculation, in order to have a better estimate of the stars' distances through an iterative process.

The iterative process stops when the new value is the same as the previous one. In other words, we wait for the convergence of the distance values. In this study we chose to stop the iterations for a given star when its new distance was less than 0.01% different from the old one, giving us a really coherent estimate of the stars' distances.

We obtain from this iterative process the distances of our red clump stars which are gathered in table C.1.

5.1.4 Distance uncertainties

In order to obtain the uncertainty in our distance estimates, we assumed independent gaussian errors for each calculated quantity in the previous iterating process. This allows us to compute the uncertainties following the propagation method where a given standard error ϵ of a function f which depends on the quantities $(\mathrm{a}, \mathrm{b}, \ldots)$ can be written as:

$$\epsilon(\mathrm{f}(\mathrm{a}, \mathrm{b}, \ldots)) = \sqrt{\sum_{\mathrm{i=a,b,...}} \left(\frac{\partial \mathrm{f}}{\partial \mathrm{i}}\right)^2 \cdot (\epsilon(\mathrm{i}))^2} \tag{5.4}$$

Dereddening

As the process is iterative, we initialise the uncertainty in distance to 0 pc, in order to have a first estimation on the dereddening uncertainties, which are, following the previous formula:

$$\epsilon(\mathrm{E}(B-V)_{\mathrm{Bon}}) = \epsilon(\mathrm{c_A}) \cdot \mathrm{E}(B-V)_{\mathrm{Bon}} \tag{5.5}$$

where:

$$\epsilon(\mathrm{c_A}) = \begin{cases} \exp(-\frac{\mathrm{d}}{125} \cdot \sin(b)) \cdot \mathrm{R} & \text{if } \sin(b) > 0 \\ \exp(\frac{\mathrm{d}}{125} \cdot \sin(b)) \cdot \mathrm{R} & \text{if } \sin(b) < 0 \end{cases} \tag{5.6}$$

[4]In their paper, the authors did not say to which solar values their metallicity had been normalised to build their calibration formula, so, in order to be self-consistent we kept our own determination of solar iron abundance for the normalisation.

with:

$$\mathrm{R} = \sqrt{\left(\frac{\sin(b)}{125}\right)^2 \cdot \epsilon(\mathrm{d})^2 + \left(\frac{\mathrm{d}}{125} \cdot \cos\left(b\right)\right)^2 \cdot \epsilon(b)^2} \tag{5.7}$$

and the galactic longitude and galactic latitude uncertainties (here we only need the latitude one) calculated from the error ellipses given in the literature, where they are given in the form [major axis ($\mathrm{m_j}$, in mas), minor axis ($\mathrm{m_i}$, in mas), position angle (p, in degrees)][5]:

$$\begin{aligned} \epsilon(l) &= \frac{\pi}{180 \cdot 3600} \cdot \sqrt{\sin^2 \mathrm{p} \cdot \mathrm{m_j^2} + \cos^2 \mathrm{p} \cdot \mathrm{m_i^2}} \\ \epsilon(b) &= \frac{\pi}{180 \cdot 3600} \cdot \sqrt{\cos^2 \mathrm{p} \cdot \mathrm{m_j^2} + \sin^2 \mathrm{p} \cdot \mathrm{m_i^2}} \end{aligned} \tag{5.8}$$

Absolute magnitude

Applying equation (5.4) to the absolute magnitude calibration formula given in equation (5.2), we have:

$$\epsilon(\mathrm{M}_V) = \frac{\sqrt{(B-V)_0^2 \cdot 0.104^2 + 0.627^2 \cdot \epsilon((B-V)_0)^2}}{+ [\mathrm{Fe/H}]^2 \cdot 0.043^2 + 0.046^2 \cdot \epsilon([\mathrm{Fe/H}])^2 + 0.111^2} \tag{5.9}$$

with $\epsilon([\mathrm{Fe/H}])$ coming from the process of abundance determination (our own values), and with $\epsilon((B-V)_0) = \left[\epsilon(B)^2 + \epsilon(V)^2 + \epsilon(\mathrm{E}(B-V)_{\mathrm{Bon}})^2\right]^{1/2}$, where $\epsilon(B)$ and $\epsilon(V)$ are given in the literature for all our stars.

Distances

The uncertainty in distances, practically computed iteratively at the same time as the distances themselves, is therefore written:

$$\epsilon(\mathrm{d}) = 2 \cdot \ln 10 \cdot \frac{\mathrm{d}}{10} \cdot \sqrt{\epsilon(V_0)^2 + \epsilon(\mathrm{M}_V)^2} \tag{5.10}$$

and can be plugged in $\epsilon(\mathrm{c_A})$ for the next iteration ; with $\epsilon(V_0) = \left[\epsilon(V)^2 + \epsilon(\mathrm{A}_V)^2\right]^{1/2}$ where $\epsilon(\mathrm{A}_V) = \left[(3.07 \cdot \mathrm{E}(B-V)_{\mathrm{Bon}})^2 \cdot \left((\frac{0.05}{3.07})^2 + (\frac{\epsilon(\mathrm{E}(B-V)_{\mathrm{Bon}})}{\mathrm{E}(B-V)_{\mathrm{Bon}}})^2\right)\right]^{1/2}$ (see McCall (2004) for the extinction ratio and its uncertainty "unlikely to exceed 0.05").

The uncertainties are gathered in table C.1 along with the distances.

5.1.5 Calculating the galactic space velocities of our stars

To obtain the space velocities (U,V,W) of our stars and their uncertainties ($\epsilon_{\mathrm{U}}, \epsilon_{\mathrm{V}}, \epsilon_{\mathrm{W}}$), we followed the method described in Johnson & Soderblom (1987). But the method was done for equatorial coordinates at epoch B1950, and we had previously gathered for our stars the galactic coordinates at epoch J2000 in order to compute their distances. Therefore, we applied a correction from ESA (1997) (Volume 1, section 1.5.3) which provides a transformation method to convert equatorial coordinates at epoch J2000 to galactic coordinates (at epoch

[5]See `http://cdsweb.u-strasbg.fr/simbad/guide/errell.htx`. Here the errors are converted from mas to rad with the pre-square-root factor.

J2000 also). Thus, we only had to inverse this method in order to get equatorial coordinates at epoch J2000 and apply then the method of Johnson & Soderblom (1987) with the transformation matrix from ESA (1997) since our values are at epoch J2000.

However, for the proper motions and respective uncertainties of our stars (needed to compute the velocities and their uncertainties) we updated our values to the UCAC4 (Zacharias et al., 2013) values which are more accurate than the proper motions and respective uncertainties taken from older papers. Indeed, UCAC4 is a newly released catalogue (in August 2012) whose observations have been proceeded in May 2004. Therefore, UCAC4 values for proper motions and uncertainties are preferred.

Step 1: coordinates transformation

We first transform galactic coordinates to equatorial coordinates (both at epoch J2000), using:

$$({\rm A_G}^{\rm t})^{-1} \begin{bmatrix} \cos b \cdot \cos l \\ \cos b \cdot \sin l \\ \sin b \end{bmatrix} = \begin{bmatrix} \cos \delta \cdot \cos \alpha \\ \cos \delta \cdot \sin \alpha \\ \sin \delta \end{bmatrix} \tag{5.11}$$

where $({\rm A_G}^{\rm t})^{-1}$ is inverse of the transpose of

$${\rm A_G} = \begin{bmatrix} -0.0548755604 & 0.4941094279 & -0.8676661490 \\ -0.8734370902 & -0.4448296300 & -0.1980763734 \\ -0.4838350155 & 0.7469822445 & 0.4559837762 \end{bmatrix} \tag{5.12}$$

which is the transformation matrix build in the ESA document, and where l and b are respectively the galactic longitude and latitude, and α and δ the equatorial right ascension and declination (all in degrees).

At this step we can check that α and δ calculated above are in agreement with values which are in fact available in either previously refereed papers or UCAC4 (which are exactly the same in both catalogues for the coordinates). Our values were all equal to the catalogue values up to 0.1 milli-degree, which confirms the accuracy of the previous transformation matrix at least for our stars' coordinates, allowing us to use this method consistently.

Step 2: space velocities calculation

Therefore, introducing:

$${\rm A} = \begin{bmatrix} \cos \alpha \cdot \cos \delta & -\sin \alpha & -\cos \alpha \cdot \sin \delta \\ \sin \alpha \cdot \cos \delta & \cos \alpha & -\sin \alpha \cdot \sin \delta \\ \sin \delta & 0 & \cos \delta \end{bmatrix} \tag{5.13}$$

and ${\rm B} = {\rm A_G}^{\rm t}{\rm A}$, we can write:

$$\begin{bmatrix} {\rm U} \\ {\rm V} \\ {\rm W} \end{bmatrix} = {\rm B} \begin{bmatrix} \rho \\ {\rm k} \cdot \mu_\alpha / \pi_{\rm a} \\ {\rm k} \cdot \mu_\delta / \pi_{\rm a} \end{bmatrix} \tag{5.14}$$

where (U,V,W) are the three components of the space velocity of a given star in km/s, with U directed towards the galactic centre, V towards the galactic rotation, and W towards the north galactic pole, ρ being its radial velocity (in km/s), π_a its parallax (in mas), μ_α and μ_δ its proper motion (in right ascension and in declination respectively, both in mas/yr), and with k = 4.7405 a constant relating mas/yr to km/s/kpc. We obtain from this computation the space velocities gathered in table C.2.

Step 3: uncertainties calculation

To compute the uncertainty in the velocities, we followed as well the method given in Johnson & Soderblom (1987). The uncertainties in (U,V,W), denoted as $(\epsilon_\mathrm{U}, \epsilon_\mathrm{V}, \epsilon_\mathrm{W})$, are obtained from the calculation of the velocities' variances:

$$\begin{bmatrix} \epsilon_\mathrm{U}^2 \\ \epsilon_\mathrm{V}^2 \\ \epsilon_\mathrm{W}^2 \end{bmatrix} = \mathrm{C} \begin{bmatrix} \epsilon_\rho^2 \\ \mathrm{k}/{\pi_\mathrm{a}}^2 \cdot [\epsilon_{\mu_\alpha}^2 + (\mu_\alpha \cdot \epsilon_{\pi_\mathrm{a}}/\pi_\mathrm{a})^2] \\ \mathrm{k}/{\pi_\mathrm{a}}^2 \cdot [\epsilon_{\mu_\delta}^2 + (\mu_\delta \cdot \epsilon_{\pi_\mathrm{a}}/\pi_\mathrm{a})^2] \end{bmatrix} + 2 \cdot \mu_\alpha \cdot \mu_\delta \cdot \mathrm{k}^2 \cdot \epsilon_{\pi_\mathrm{a}}^2/\pi_\mathrm{a}^4 \begin{bmatrix} \mathrm{b}_{12} \cdot \mathrm{b}_{13} \\ \mathrm{b}_{22} \cdot \mathrm{b}_{23} \\ \mathrm{b}_{32} \cdot \mathrm{b}_{33} \end{bmatrix} \quad (5.15)$$

where $\mathrm{b_{ij}}$ are elements of the matrix B from Step 2, the elements of the matrix C are the squares of the individual elements of B (for all i and j : $\mathrm{c_{ij}} = \mathrm{b_{ij}^2}$), ϵ_ρ is the standard error in radial velocity (in km/s, computed both from the uncertainties from TAME and our RV correction), ϵ_{π_a} the uncertainty in parallax (in mas, computed by the propagation method from the distances and their errors calculated previously[6]), ϵ_{μ_α} and ϵ_{μ_δ} the uncertainties in proper motions (in mas/yr, respectively in right ascension and declination). The uncertainties are gathered in table C.2 along with the velocities.

5.1.6 Galactic orbits

The galactic orbits and related parameters ($\mathrm{R_{min}}$, $\mathrm{R_{max}}$, $\mathrm{z_{min}}$, $\mathrm{z_{max}}$, $\mathrm{L_z}$, E) of our stars were calculated with a numerical integrator[7] of time-span 600 Myr (into the future), using a Paczyński potential (Paczyński & Wiita, 1980), and heliocentric positions and velocities of our stars as input. With $\mathrm{R_{min}}$ and $\mathrm{R_{max}}$, in pc, being the galactocentric radii at the periapsis and apoapsis respectively (least and greatest distances), $\mathrm{z_{min}}$ and $\mathrm{z_{max}}$, in pc, being the least and greatest vertical distances above or below the galactic plane at farthest points, $\mathrm{L_z}$, in $\mathrm{pc \cdot km/s}$, the angular momentum, and E, in $\mathrm{km^2/s^2}$, the energy. These parameters are gathered in table C.3.

5.2 Inferring stars' dynamical properties

5.2.1 Velocity distribution

According to several papers, stars believed to belong to the thick disc population have in average higher peculiar velocities than those believed to belong to the thin disc. Indeed, Bensby et al. (2003) showed that stars with probabilities ten times higher of belonging to a

[6] Since $\pi_a = 1000/\mathrm{d}$, with π_a in mas and d in pc, we have : $\epsilon(\pi_\mathrm{a}) = \sqrt{(1000/\mathrm{d}^2)^2 \cdot \epsilon(\mathrm{d})^2} = 1000/\mathrm{d} \cdot \epsilon(\mathrm{d})$.

[7] Whose script was provided by Lennart Lindegren under MATLAB and slightly modified for the purpose of this study.

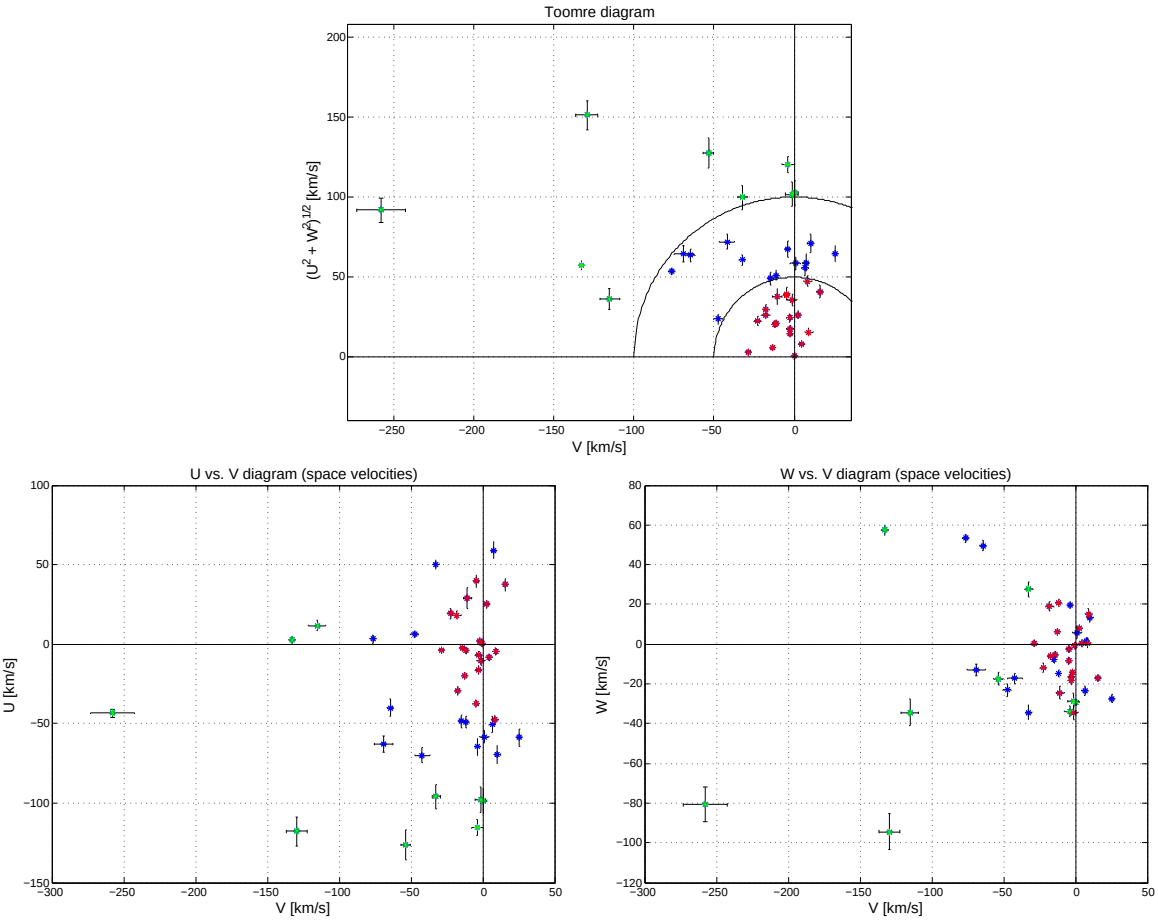

Figure 5.2: Top panel: Toomre diagram of our 43 red clump stars, centred on the sun. Black half circle lines indicate constant peculiar velocities of 50 km/s and 100 km/s. Colours are given as mentioned in §5.2.1 page 33. Uncertainties are also shown, and re-calculated accordingly to the propagation method for the y-axis[8]. Bottom left panel: space velocity diagram in (V,U), with uncertainties and colour labels. Bottom right panel: space velocity diagram in (V,W), with uncertainties and colour labels.

thick disc population rather than to the thin disc all had peculiar space velocities higher than about 100 km/s, whereas stars with probabilities ten times lower of belonging to a thick disc population rather than to the thin disc mostly had peculiar space velocities lower than 50 km/s; where the peculiar space velocity of a given star is defined as : $v_p = \sqrt{U^2 + V^2 + W^2}$. Therefore, we labeled our stars that have $v_p \leq 50$ km/s with a particular colour (we chose red) and those that have $v_p \geq 100$ km/s with another colour (we chose green), the stars in between being blue by default, see top panel figure 5.2. Hence, this labelling will help us to see in coming investigations if stars with different kinematics have different abundances and how their properties differ. Nevertheless, we have to remember that Bensby et al. (2014), for instance, showed that there is no absolute kinematic way to discriminate between thin and thick disc stars since there is a large kinematic overlap between the two suspected populations.

As we see in the bottom panels of figure 5.2, stars with the coldest kinematics (labelled in red) have tangential (V), radial (U) and vertical (W) velocity components similar to the sun

[8]If we note $\beta = \sqrt{U^2 + W^2}$, then we have $\epsilon(\beta) = 1/\beta \cdot \sqrt{U^2 \cdot \epsilon(U)^2 + W^2 \cdot \epsilon(W)^2}$

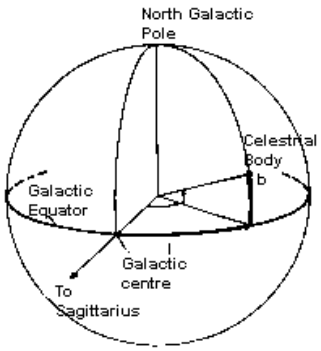

Figure 5.3: Galactic coordinate system as used in this work. The system is centred on the sun. l the galactic longitude and b the galactic latitude are shown. In order to have positions in cartesian heliocentric coordinates, we define (x,y,z) axes as follow: the x-axis points towards the galactic centre, the y-axis points towards the direction of the sun's rotation around the galactic centre (to the right here), and the z-axis points towards the north galactic pole.

and are roughly evenly spread around the sun's values, whereas stars with warmer kinematics (in green) all lag behind the sun in tangential velocity, and of more than 100 km/s for 4 of them (among 9), which is one more argument in favour of believing that warmly kinematical stars are more likely to belong to the thick disc population since several papers have found a rotationally lagging thick disc with respect to the sun. For instance, Soubiran et al. (2003) found a moderate rotational lag of 51 ± 5 km/s behind the sun for the thick disc. They also found a higher dispersion in the velocity components around their mean values with $(\sigma_{\mathrm{U}}, \sigma_{\mathrm{V}}, \sigma_{\mathrm{W}}) = (63\pm6, 39\pm4, 39\pm4)$ km/s for the thick disc against $(39\pm2, 20\pm2, 20\pm1)$ km/s for the thin disc. In our plots, we clearly see that the dispersions in U, V and W are higher for the green stars and the lowest for the red ones, which, according to the cited paper, gives credit to consider that green stars are likely to be in majority thick disc stars while red ones are likely to be in majority thin disc stars. In fact, we have here $(\sigma_{\mathrm{U}}, \sigma_{\mathrm{V}}, \sigma_{\mathrm{W}}) = (53 \pm 3, 86 \pm 4, 47 \pm 3)$ km/s for the green stars and $(\sigma_{\mathrm{U}}, \sigma_{\mathrm{V}}, \sigma_{\mathrm{W}}) = (24 \pm 1, 11 \pm 1, 14 \pm 1)$ km/s for the red ones (the blue stars in between give $(\sigma_{\mathrm{U}}, \sigma_{\mathrm{V}}, \sigma_{\mathrm{W}}) = (44 \pm 1, 33 \pm 1, 27 \pm 1)$ km/s).

5.2.2 Positions

The positions of our stars relative to the sun, and their uncertainties, can be computed from the distances and galactic coordinates (longitude and latitude). We choose to build our cartesian heliocentric coordinate system according to the right handed rule, with the x-axis increasing towards the galactic centre, the y-axis increasing towards the direction of the sun's rotation around the galactic centre, and with the z-axis in the direction of the north galactic pole, see figure 5.3. The conversion between galactic coordinates and our cartesian heliocentric coordinates is:

$$\begin{bmatrix} \mathrm{X} \\ \mathrm{Y} \\ \mathrm{Z} \end{bmatrix} = \mathrm{d} \cdot \begin{bmatrix} \cos b \cdot \cos l \\ \cos b \cdot \sin l \\ \sin l \end{bmatrix} \tag{5.16}$$

Therefore, uncertainties are given by:

$$\begin{bmatrix} \epsilon(\mathrm{X}) \\ \epsilon(\mathrm{Y}) \\ \epsilon(\mathrm{Z}) \end{bmatrix} = \begin{bmatrix} \sqrt{(\cos l \cdot \sin b \cdot \mathrm{d})^2 \cdot \epsilon(b)^2 + (\cos b \cdot \sin l \cdot \mathrm{d})^2 \cdot \epsilon(l)^2 + (\cos b \cdot \cos b)^2 \cdot \epsilon(\mathrm{d})^2} \\ \sqrt{(\sin l \cdot \sin b \cdot \mathrm{d})^2 \cdot \epsilon(b)^2 + (\cos b \cdot \cos l \cdot \mathrm{d})^2 \cdot \epsilon(l)^2 + (\cos b \cdot \sin l)^2 \cdot \epsilon(\mathrm{d})^2} \\ \sqrt{(\cos b \cdot \mathrm{d})^2 \cdot \epsilon(b)^2 + \sin b^2 \cdot \epsilon(\mathrm{d})^2} \end{bmatrix} \tag{5.17}$$

Stars' current distances and positions are not correlated to kinematics as we can see in figure 5.4, where we have plotted the stars' positions with the colour labels according to their kinematics. Both stars with warm (higher values) and cold (lower values) kinematics are evenly spread in distance and position. Thus, our sample is kinematically unbiased as we have neither preferentially observed one kinematical population (warm or cold) over the other one when increasing the distance of observation nor tried to do so in order to increase the presence of one kinematic population at a given location. In other words, we have not selected against stars with cold kinematics at high latitudes nor stars with warm kinematics at low latitudes (or the contrary). Therefore, our sample is representative of the real stars' kinematic distribution at the observed locations, hence we are not likely to infer biased properties for our stars (like highlighting a dichotomy in a given distribution whereas its change is smooth in reality).

5.2.3 Further investigation

In the plots of the positions of the stars figure 5.4, we clearly discern two groups of stars corresponding to the two observing runs. One group, the most populated one with 32 stars, is located near X = 0 pc, we denote it group 1; another group, less populated with 11 stars, is located at $150 < \mathrm{X} < 300$ (in pc), we denote it group 2. The two groups being located relatively far from each other in the radial direction, with group 2 closer to the galactic centre, it appears physically interesting to investigate the properties of these two groups also separately.

Thus, we show figure 5.5 the peculiar velocities of the stars according to a colour labelling discerning the two groups. We see that group 2 stars have no particular velocities, which means that they do not belong to a particular moving group. However, it is still interesting to keep this extended colour labelling (black for group 1 stars and magenta for group 2 stars), since studying the two groups separately gives us the opportunity to investigate the constancy of the abundance trends at different locations in the radial direction of the galactic plane within our sample.

5.3 Conclusions

The aim of this chapter was to determine the kinematic properties of our red clump stars. To do so, we first gathered all the relevant informations already available in the literature, that is to say: coordinates, proper motions, and B and V magnitudes, available for all stars, radial velocity for 14 of them, as well as their respective uncertainties. Then, comparing radial velocities from the literature and those obtained with TAME from the lines' shifts and applying a barycentric correction, we determined the true radial velocity for all our stars. Next, we

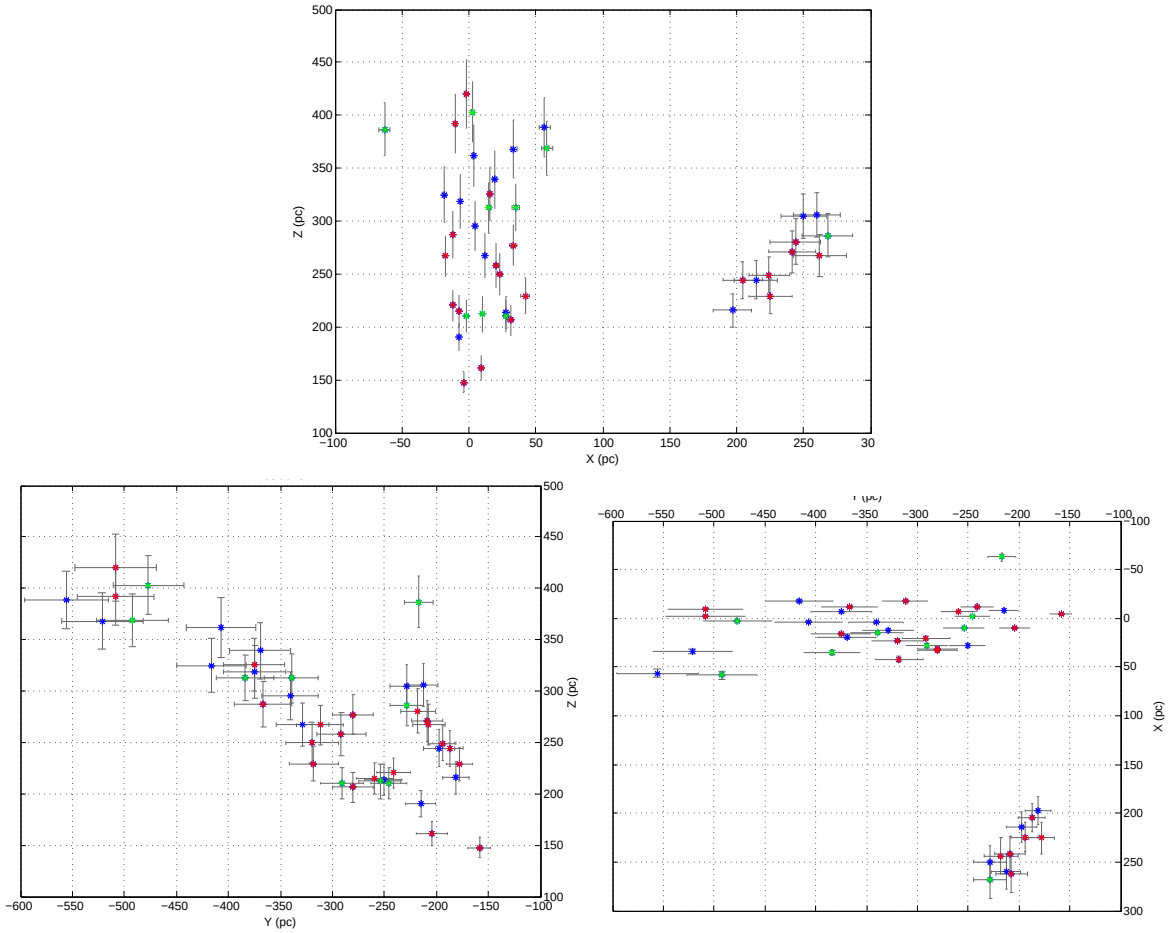

Figure 5.4: Projection of the stars' positions in the 2-D spaces (X,Z) (top panel), (Y,Z) (bottom left panel), and (Y,X) (bottom right panel), with respect to the sun. X increases towards the galactic centre, Y increases towards the direction of the sun's rotation, and Z in the direction of the north galactic pole. Colours are the kinematic labels: red for stars with $v_p \leq 50$ km/s, green for stars with $v_p \geq 100$ km/s, blue for stars in-between. Uncertainties in positions are also shown.

calculated the distances of the stars through an iterative computation based on the stellar coordinates and fluxes, the dust distribution inside the Milky Way that redden the colour of the stars, their absolute magnitude calculated using the stars' colours and metallicities, and the distance modulus linking distances to dereddened apparent and absolute magnitudes. Uncertainties were computed at the same time using the propagation method. Next, space velocities and their uncertainties were calculated from the stars' coordinates, radial velocities, distances (practically parallaxes), proper motions, and respective uncertainties. Lastly, orbital parameters were computed using a numerical integrator needing heliocentric positions and velocities as input.

This enabled us to infer purely kinematic properties for our red clump stars: based on their peculiar space velocities, we assigned our stars to a colour label corresponding to a greater likelihood of belonging to a thin disc, thick disc, or in-between population according to previous studies. Stars with $v_p \leq 50$ km/s have a high likelihood of being thin disc stars (labeled as red in figures 5.2 and 5.4), while those with $v_p \geq 100$ km/s have a high likelihood

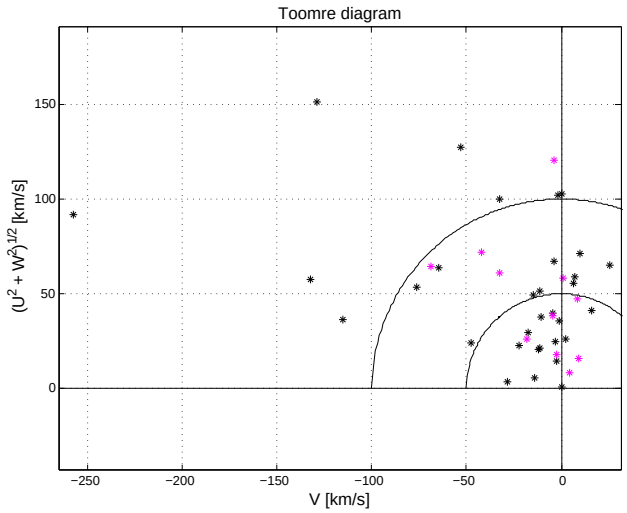

Figure 5.5: Same digram as in top panel figure 5.2 but discerning here group 1 stars from group 2 stars. Group 1 stars (X around 0 pc) are coloured in black. Group 2 stars ($150 < X < 300$, in pc) are coloured in magenta. No particular locations are taken by one group or the other: neither group forms a kinematic group. Uncertainties are not shown but are the same as in the cited figure.

of being thick disc (shown as green points). Previous studies reporting a lagging thick disc behind the sun in tangential velocity and a greater dispersion of the thick disc space velocities compared to thin disc stars tended to confirm the likelihoods of the assignments. We also verified the positions of the stars: towards the north galactic pole, at solar galactocentric radius, farther away than the solar neighbourhood, and looked at their positions according to the colour labels: current stars positions (as probed) were found to have no correlation with their kinematics (colour labels). Finally, the stars' positions showed a particular distinction into two groups having different radial position: one group being around $X = 0$ pc with respect to the sun and labelled in black, and the other one being located at $150 < X < 300$ pc towards the galactic centre and labelled in magenta. The investigation of the stars' kinematics according to these two groups did not highlight a moving group or a particular trend.

Chapter 6

Investigations

In chapter 4 we determined for each of the 43 red clump stars the chemical abundances of 16 elements from their photospheres, allowing us to infer chemical properties of our stars. In chapter 5 we determined the real distances and locations of the targeted stars, verified that they were located in the direction of the north galactic pole and farther than the solar neighbourhood, and we finally determined their velocities, and orbital properties allowing us to infer dynamical properties of our stars. Given that, we are now able to investigate how the abundances and kinematics correlate.

At first glance, no obvious inference can be drawn from the abundances of the α-elements (Ca, Mg, O, Si, Ti) and the light element Al (which behaves as an α-element relative to Fe[1]) with the colour labelling from the kinematics of the stars (see figure 6.1), exept that 4 green, 1 blue, and 0 red stars have metallicity below -0.4 dex and that they are α-enhanced. However, we have to remember that the colour labelling is only here to help the eye and indicate a likely higher probability of affiliation to one or the other population according to the results of previous studies. Therefore, we need to investigate further the relations between abundances and kinematics in order to obtain better discriminants if there are any. So far, the suspected thin and thick discs have been the better discriminated by their different scale heights, thus, the maximum height above of below the plane reached by the stars seems a legitimate feature to investigate relatively to abundance since abundances have been reported to be different in the thin and the thick discs (for instance, see Bensby et al., 2014 and Toyouchi & Chiba, 2014, for recent work, which show an α-enhanced thick disc at poor metallicity). Eccentricity of the orbits is likely to be correlated to the maximum height of the stars, but is also investigated relatively to abundances since thick disc stars are suspected to have a broader range of orbits and thus are more prone to differ from circular orbits.

6.1 α-enhancement as a function of eccentricity

The eccentricity is defined as :

$$e = \frac{R_{max} - R_{min}}{R_{max} + R_{min}} \tag{6.1}$$

with R_{max} and R_{min} from table C.3. Since the suspected thin disc has, according to previous studies, a distribution of stars more confined around the galactic plane compared to

[1]See for instance Bensby et al. (2003), and Bensby et al. (2014) for matching behaviour.

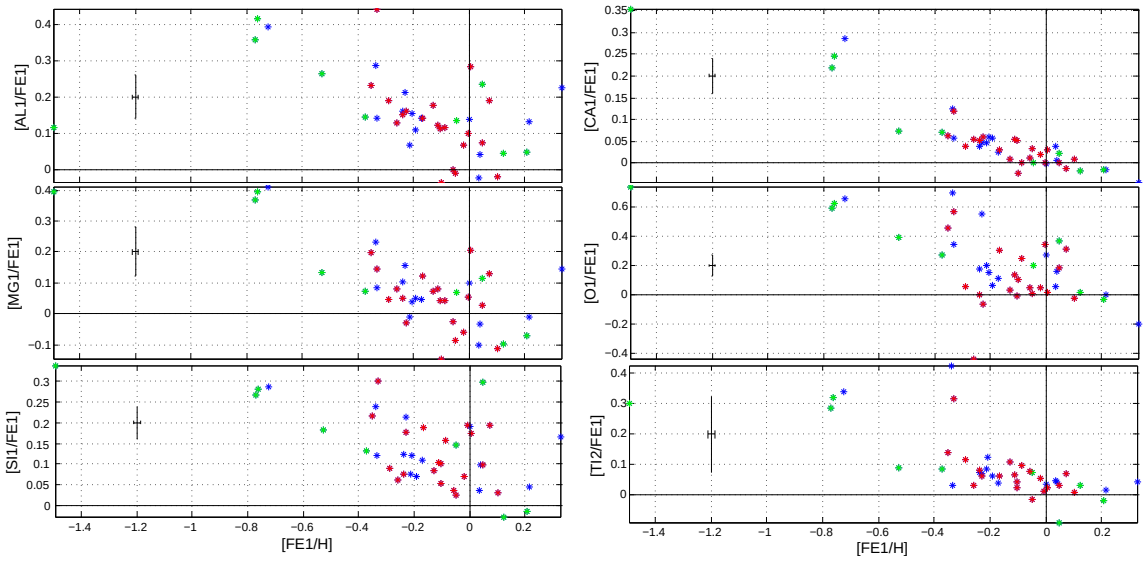

Figure 6.1: Abundance plots of the α-elements, and the light element Al, versus metallicity. Colours are the kinematic labelling: red for stars with $v_p \leq 50$ km/s, green for stars with $v_p \geq 100$ km/s, and blue in-between.. At first glance, no explicit trends are seen regarding the colour labelling. Typical internal errors are also shown, calculated from the line-to-line scatter and the number of lines used to get the mean abundances with AMOOG.

the distribution of thick disc stars, then thick disc stars are expected to have greater eccentricities in average. Therefore, the more we select stars with high eccentricity, the more the selected sub-sample is likely to contain more thick disc candidates than thin disc ones. In that way, we have in figure 6.2 ploted the abundances of the α-elements and Al (considered as an α-element hereinafter) versus [Fe/H], according to different intervals of eccentricity.

The first interval, gathering the stars with the lowest eccentricities up to 0.1, contains only red labeled stars. Those near orbitally circular stars with cold kinematics are confined in a relatively small region of metallicity with $-0.3 < [Fe/H] < 0.1$ and are not enhanced in α-elements. However, the second interval, with eccentricities from 0.1 to 0.3, gathers stars from all labels (with a majority of blue labelled stars), and starts to show a higher α-abundance which seems to increase with decreasing metallicity (particularly distinct in the calcium behaviour). As for the third interval, for eccentricities greater than 0.3, almost only green labelled stars are present, there is a clear enhancement in α-abundance, the metallicity range is much wider than in the two previous intervals with a metallicity peak around -0.5 dex and one star reaching -1.5 dex in [Fe/H]. Moreover, the increase in α-abundance is clearly correlated to a decrease in metallicity until approximately -0.7 dex in [Fe/H] where then the trend in α-abundance is flat with decreasing metallicity.

6.2 α-enhancement as a function of maximum height

6.2.1 Visual investigation

The scale height of the suspected thin disc is assumed to be approximately 300 pc, whereas the scale height of the suspected thick disc is assumed to be approximately 1000-1300 pc

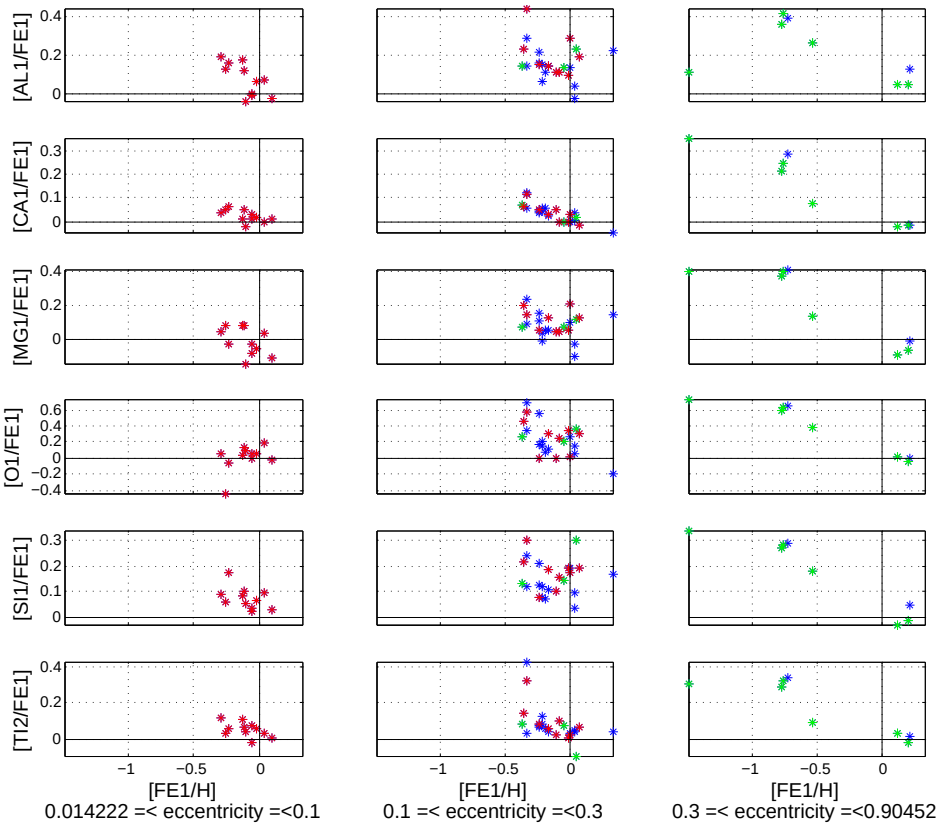

Figure 6.2: Abundance plots of the α-elements, and the light element Al, versus metallicity, for different eccentricity intervals, where the eccentricity is defined as : $e = (R_{max} - R_{min})/(R_{max} + R_{min})$, with R_{max} and R_{min} from table C.3. Colours are the kinematic labelling: red for stars with $v_p \leq 50$ km/s, green for stars with $v_p \geq 100$ km/s, and blue in-between.

(Feltzing et al., 2003). Then, thick disc stars are expected to have greater maximum height (above or below the plane) in average. We define this maximum height, z_{max}, as the maximum between $|z_{min}|$ and z_{max} from table C.3. Therefore, the more we select stars with high z_{max}, the more the selected sub-sample is likely to contain more thick disc candidates than thin disc ones. In that way, we have in figure 6.3 ploted the abundances of the α-elements and Al (considered as an α-element hereinafter) versus [Fe/H], according to different intervals of z_{max}.

In the mentioned figure, we chose the first interval so as to select only stars really confined near the galactic plane in order to have a majority of thin disc candidates over thick disc ones. Thus z_{max} goes up to 300 pc for the first interval which behaves as described for the first interval in eccentricity: no α-enhancement, and near solar metallicity (in this sub-sample we also have a few blue labeled stars whereas we had any in the first interval in eccentricity). For the second interval, we chose for the upper limit the approximate height where both suspected populations are equally represented according to previous studies. We see that stars of all kinematics (all labels) are present in this plot. However, a clear trend, particularly for calcium, is shown: stars belonging to this interval are in average much more α-enhanced than stars from the first interval, and moreover, the abundance in α-elements increases with decreasing metallicity. Also, the metallicity peak is around -0.3 dex for this interval while it is near

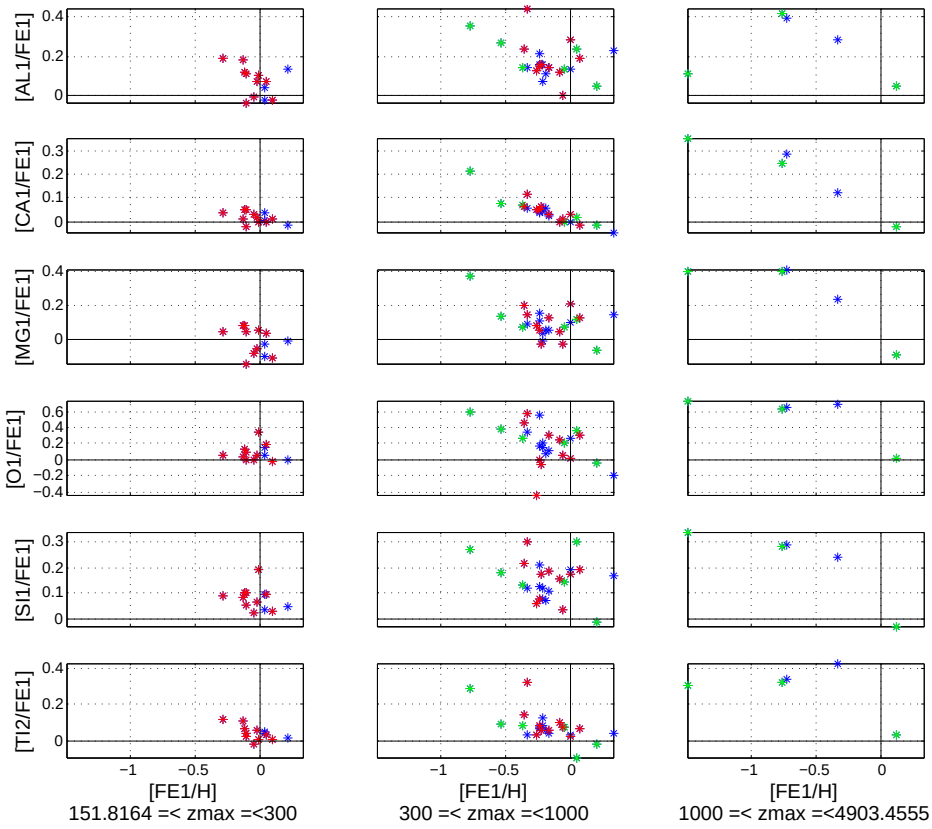

Figure 6.3: Abundance plots of the α-elements, and the light element Al, versus metallicity, for different z_{max} intervals, where z_{max} is here the maximum between z_{max} and $|z_{min}|$ from table C.3. Colours are the kinematic labelling: red for stars with $v_p \leq 50$ km/s, green for stars with $v_p \geq 100$ km/s, and blue in-between.

solar metallicity for the first interval. For the third interval, where we expect to have more thick disc candidates than thin disc candidates, the stars clearly draw a nice shaped common trend among all the α-elements. We, again, see that those stars are α-enhanced and that this enhancement increases with decreasing [Fe/H] until a flat trend at constant α-enhancement; also, the peak in metallicity, below -0.5 dex, is the lowest among the intervals.

6.2.2 Refined approach

The previous approach allowed us to distinguish different behaviours in the abundance trends of the stars according to their maximum height. However, as seen in §5.2.3, our sample of stars shows two groups having distinct radial positions. Therefore, we investigate the α-enhancement as a function of z_{max} according to the two groups. Moreover, in order to distinguish how smooth or steep is the change from one trend to the other, we compute a refined approach.

First improvement, instead of setting intervals that do not overlap, we select stars in an interval of relatively tiny amplitude in height (50 pc) which scans all stars by small steps (of 10 pc) with the condition to have a sufficient number of stars (we chose 5) at each stage in order to compute a mean abundance and a mean position within each interval all along the

scanning process; the amplitude of the scanning interval being increased in the case of too few stars in a given interval, until the condition is reached. Moreover, the new approach takes into account the uncertainty in the vertical position of the stars. For instance, a star with, say, $z_{max} = 310 \pm 30$ pc, will be taken into account in all intervals having their lower boundary below $310 + 30$ pc and upper boundary over $310 - 30$ pc. We can note that, as we consider an interval with small amplitude which scans the positions of the stars with a really small step, it is important to care for the uncertainty in the vertical position; however, for the visual approach, even if such a star should have been represented in the first and second intervals, it would not have changed the shapes of the trends considering the very little amount of stars likely to belong to two of such wide intervals. Group 1 stars and group 2 stars are also treated separately.

Figure 6.4 shows the results of the just explained computation of the refined approach. Each point along the curves represents the mean vertical position for the x-axes (both Z and z_{max} are plotted for comparison) and the mean abundance of three compounds for the y-axes, of the stars included in the considered scanning interval at that step. The error bars in the x-axes represent the scatter in vertical position for each interval where the mean has been computed. Indeed, we chose to represent the scatter in order to have a visual estimation of the amplitude of each interval, rather than the precision in the stars' positions in each interval, since the precision is really good but gives no information about the intervals used. Nevertheless, the error bars in the y-axes are the error in the mean[2] (sometimes called formal error) of each interval since we want to know the precision of the mean abundance of the stars considered at each step in order to be able to distinguish a trend, a behaviour, in abundance as a function of height, as well as whether group 1 and group 2 stars are statistically different.

As we can see, the plots of abundances versus Z show no particular trend since the curves are statistically not different from being flat due to the uncertainties in the mean abundance of each interval. In the same way, group 1 stars and group 2 stars cannot be viewed as having different behaviours since their error bars in abundances are overlapping most of the time. However, we see clear trends in the plots of the abundances versus z_{max}. Indeed, as explained in §5.2.2 page 35 the current Z positions of the different star candidates are all mixed. Therefore, the mean abundance of a given interval should not be significantly different from any other one: it is what we see in the plots. So, when looking for discriminants in the study of the galactic vertical distribution of stars, the importance of choosing to investigate stellar behaviours according to the stars' maximum height rather than their current height is not negligible. Indeed, we see here that in the right column plots which consider z_{max} (still figure 6.4), the abundance curves give significantly different results than when considering Z (left column plots).

For group 1 stars, when considering stars whose maximum heights are below $10^{2.5}$ (or approximately 300) parsecs, where we have a majority of thin disc candidates over thick disc candidates, we distinguish a small drop in metallicity, and an increase in α-abundances. Then, until approximately $10^{2.9}$ (800) parsecs, we see a region where metallicity as well as α-abundances shifts unevenly. This is due to a few outliers moving the mean abundance drastically in a given interval. However, for group 2 stars, outliers are not observed, and the

[2]The uncertainty in the abundance of the stars, for each element, which is the line-to-line scatter from the computation of the mean abundances with AMOOG, is, for stars in a same interval, squared, summed to each other, rooted, and divided by the number of stars in the considered interval.

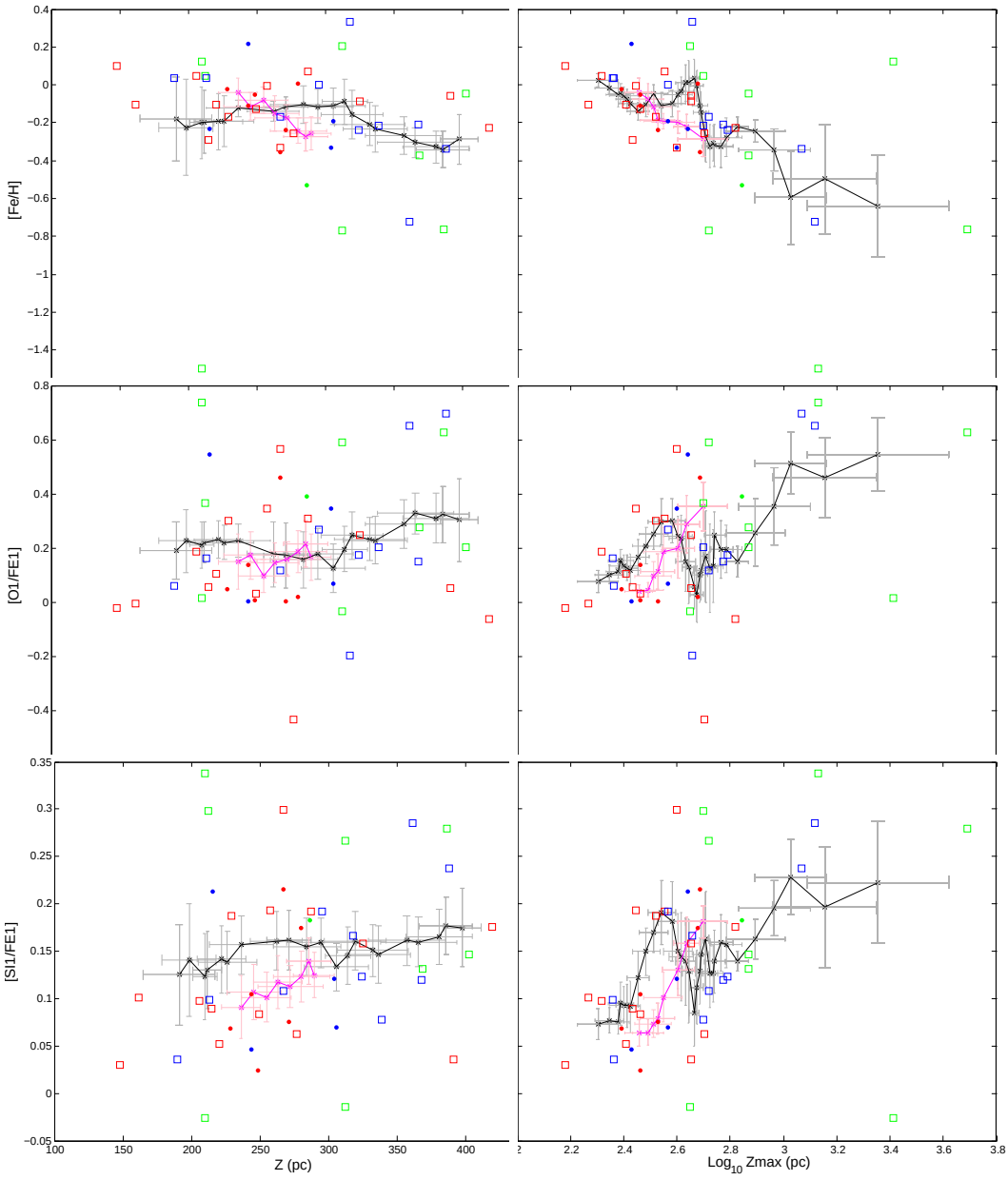

Figure 6.4: Plots of the refined approach, as described in §6.2.2. We have for the y-axes, from top to bottom: the metallicity, the oxygen abundance, and the silicon abundance. For the x-axes, from left to right, we have Z, and $\log z_{max}$ respectively. The black line is associated to group 1 stars, the magenta line to group 2 stars. Empty squares are the individual values of group 1 stars, and filled dots are the individual values of group 2 stars, both with kinematic colour labelling: red for stars with $v_p \leq 50$ km/s, green for stars with $v_p \geq 100$ km/s, and blue in-between. See §6.2.2 for the descriptions of the error bars (grey for group 1 stars, pink for group 2 stars).

abundance trends of these stars are clearly defined. Indeed, we see a clear drop in metallicity, and a clear increase in α-abundances as we increase in maximum height, in other words, as we have more and more thick disc candidates in a given interval. Uncertainties in abundances of group 2 stars do not impede this behaviour. Furthermore, for group 1 stars, over a maximum

height of 800 pc, where thick disc candidates approximately start to be more represented than thin disc candidates, we again clearly see a constant drop in metallicity, and a constant increase in α-abundances only impeded by one or a very few outliers.

6.3 α-enhancement as a function of space velocity

Soubiran et al. (2003) found that the thick disc was lagging behind the sun in tangential (V) velocity. Therefore, it is legitimate to investigate how abundances correlate with V among our sample of stars. We adopted the refined approach as described in §6.2.2 and applied it to the tangential velocity of our star instead of Z or z_{max}.

We see figure 6.5 that the more stars lag behind the sun, the poorer the metallicity. Moreover, the α-abundance increases as the stars lag behind the sun. In the plots we see that stars near solar V have either a flat near solar abundance (for Ca and Fe) or have a wide range of abundances (for O and Si) that show no particular trend. However, as we select stars with warmer V velocity, typically for a lag above 50 km/s, then the clear trends are shown. Also, group 1 stars and group 2 stars are not different in their common range of velocity varying from 40 to -50 km/s with respect to the sun. Therefore, based on the previous results of this study, stars that lag behind the sun show a chemical behaviour associated to a high thick disc likelihood, while stars near solar V have a chemical behaviour associated to a high thin disc likelihood.

6.4 Conclusions

The aim of this chapter was to investigate the possible correlations between the abundances and kinematics determined in this study. We particularly looked at how abundances were correlated to eccentricities, heights and tangential velocities. To do so, we first implemented a 'visual' approach consisting of analysing the α-abundance trends of stars selected in distinct and wide intervals of eccentricities or maximum height. This showed that the more likely we were selecting thick disc candidates, the more stars were α-enhanced and had low metallicity in average. We then implemented a 'refined' approach consisting of analysing the α-abundances and metallicity as a function of current height, maximum height, and tangential velocity. Current heights, not really representative of the stars' kinematic and orbital properties, showed constant mean abundances. However, maximum heights, more representative of the stars' kinematics and orbital properties, showed a clear increase in α-abundances and a clear decrease in metallicity for group 2 stars and only impeded by a few outliers for group 1 stars. Tangential velocity showed a clear trend for group 1 stars: α-enhancement and poorer metallicity as stars lag behind the sun, however tangential velocities of group 2 stars where more mixed and not correlated to z_{max} as they did not show the clear trends as seen for z_{max}, but mean abundances. Therefore, z_{max} appears to be a better discriminant.

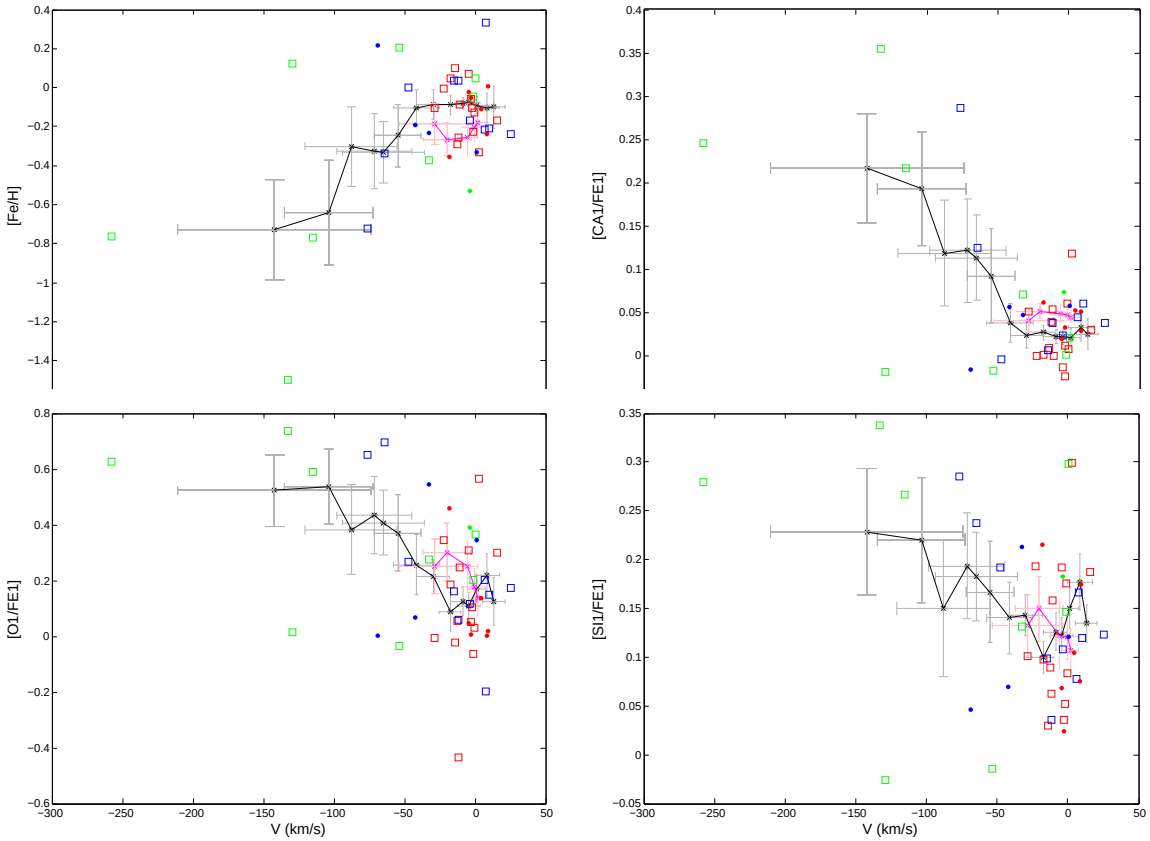

Figure 6.5: Plots of the abundances versus V, under the refined approach. We have for the y-axes, from top to bottom and left to right: the metallicity, the calcium abundance, the oxygen abundance, and the silicon abundance. The black line is associated to group 1 stars, the magenta line to group 2 stars. Empty squares are the individual values of group 1 stars, and filled dots are the individual values of group 2 stars, both with kinematic colour labelling: red for stars with $v_p \leq 50$ km/s, green for stars with $v_p \geq 100$ km/s, and blue in-between. See §6.2.2 for the descriptions of the error bars (grey for group 1 stars, pink for group 2 stars).

Chapter 7

Conclusion

The aim of this thesis was to answer the question: do the different chemical and kinematic trends seen locally and attributed to either the thin or the thick disc persist outside the solar neighbourhood? To solve this issue we relied on the spectra of 43 red clump stars. Using tools of spectra analyses we determined for each star the atmospheric parameters $T_{\rm eff}$, $\log g$ and $V_{\rm t}$, and the abundances of the following 16 elements: AlI, BaII, CaI, CrI, CrII, FeI, FeII, MgI, NaI, NiI, OI, SiI, TiI, TiII, YII, and ZnI. We found our red clump abundances to be consistent with abundance behaviours of other red clump and dwarf stars selected in the solar neighbourhood. We notably found stars to have the characteristic α-enhanced behaviour at poor metallicity, described as highly likely specific of thick disc stars in the studies probing the solar neighbourhood. Using the literature, our own data, and dust maps, we then determined the positions, space velocities, and orbital parameters of our stars. We found that our sample was actually located outside the solar neighbourhood, and that the majority of the stars had near solar space velocities, below 50 km/s with respect to the sun, while a small handful had peculiar velocities above 100 km/s with respect to the sun, the later being described as highly likely specific of thick disc stars in the studies probing the solar neighbourhood. We colour labelled the stars according to these groups and found no apparent correlation between actual positions and kinematics. We finally investigated the abundance-kinematic relations and found that the eccentricity and maximum height, below or above the plane, of the stars were correlated to abundances in the following way: the more a star is orbitally eccentric or the more its maximum height is high, the more the star deviates from near solar abundances and shows an α-enhanced behaviour at poor metallicity. We found the same tendency the more stars are rotationally lagging behind the sun; this lagging being again described as highly likely specific of thick disc stars in the studies probing the solar neighbourhood.

Outside the solar neighbourhood, our study showed that, on the one hand, stars kinematically near solar dynamics, and having a high kinematic thin disc likelihood, had also abundances associated locally to thin disc stars. On the other hand, stars kinematically deviating from solar dynamics, and having a high kinematic thick disc likelihood, had also specific abundance behaviours associated locally to thick disc stars. Therefore, our findings demonstrate that the abundance trends seen locally, and distinguishing the thin and the thick disc, most likely persist outside the solar neighbourhood.

Bibliography

Asplund, M., Grevesse, N., Sauval, A. J., & Scott, P. 2009, ARA&A, 47, 481

Bensby, T., Alves-Brito, A., Oey, M. S., Yong, D., & Meléndez, J. 2010, A&A, 516, L13

Bensby, T., Feltzing, S., & Lundström, I. 2003, A&A, 410, 527

Bensby, T., Feltzing, S., & Oey, M. S. 2014, A&A, 562, A71

Bernstein, R., Shectman, S. A., Gunnels, S. M., Mochnacki, S., & Athey, A. E. 2003, Proc. SPIE, 4841, 1694

Bilir, S., Ak, T., Ak, S., Yontan, T., & Bostancı, Z. F. 2013, New Astronomy, 23, 88

Bonifacio, P., Monai, S., & Beers, T. C. 2000, AJ, 120, 2065

Cabrera-Lavers, A., Garzón, F., & Hammersley, P. L. 2005, A&A, 433, 173

Demarque, P., Woo, J.-H., Kim, Y.-C., & Yi, S. K. 2004, ApJS, 155, 667

Edvardsson, B., Andersen, J., Gustafsson, B., et al. 1993, A&A, 275, 101

ESA 1997, The Hipparcos and Tycho Catalogues, ESA SP-1200

Feltzing, S., Bensby, T., & Lundström, I. 2003, A&A, 397, L1

Gilmore, G., & Reid, N. 1983, MNRAS, 202, 1025

Gilmore, G., Wyse, R. F. G., & Kuijken, K. 1989, ARA&A, 27, 555

Gontcharov, G. A. 2006, Astronomy Letters, 32, 759

Gray, D. F. 2008, The Observation and Analysis of Stellar Photospheres, by David F. Gray, Cambridge, UK: Cambridge University Press, 2008

Grevesse, N., & Sauval, A. J. 1998, Space Science Reviews, 85, 161

Griffin, R. F., & Cornell, A. P. 2006, MNRAS, 371, 1140

Grocholski, A. J., & Sarajedini, A. 2002, AJ, 123, 1603

Høg, E., Fabricius, C., Makarov, V. V., et al. 2000, A&A, 355, L27

Høg, E., Kuzmin, A., Bastian, U., et al. 1998, A&A, 335, L65

Johnson, D. R. H., & Soderblom, D. R. 1987, AJ, 93, 864

Kang, W., & Lee, S.-G. 2012, MNRAS, 425, 3162

van Leeuwen, F. 2007, A&A, 474, 653

Magrini, L., Randich, S., Friel, E., et al. 2013, A&A, 558, A38

McCall, M. L. 2004, AJ, 128, 2144

Mishenina, T. V., Bienaymé, O., Gorbaneva, T. I., et al. 2006, A&A, 456, 1109

Paczyński, B., & Stanek, K. Z. 1998, ApJ, 494, L219

Paczyński, B., & Wiita, P. J. 1980, A&A, 88, 23

Pietrzyński, G., Gieren, W., & Udalski, A. 2003, AJ, 125, 2494

Schlegel, D. J., Finkbeiner, D. P., & Davis, M. 1998, ApJ, 500, 525

Soubiran, C., Bienaymé, O., & Siebert, A. 2003, A&A, 398, 141

Spitzer, L. 1978, New York Wiley-Interscience, 1978. 333 p.

Stanek, K. Z., & Garnavich, P. M. 1998, ApJ, 503, L131

Toyouchi, D., & Chiba, M. 2014, arXiv:1405.0405

Zacharias, N., Finch, C. T., Girard, T. M., et al. 2013, AJ, 145, 44

Zwitter, T., Siebert, A., Munari, U., et al. 2008, AJ, 136, 421

Appendix A

Abundances and stellar parameters

For each element X in tables A.1 and A.2, the abundances are expressed as: $\mathrm{X} = \log\left(\frac{\mathrm{N_X}}{\mathrm{N_H}}\right)_\star$, as given by AMOOG output.

Table A.1: Abundances

Object	Al	BaII	Ca	CrI	CrII	FeI	FeII	Mg	Na	Ni	O	Si	TiI	TiII	YII	Zn
Sun	6.64	2.34	6.49	5.77	5.78	7.68	7.64	7.89	6.39	6.38	8.77	7.61	5.11	5.09	2.33	4.66
HD094928	6.56	2.15	6.29	5.57	5.47	7.44	7.41	7.76	6.27	6.17	8.70	7.50	4.96	4.92	2.10	4.78
HD095179	6.90	2.34	6.55	5.92	6.09	7.75	7.71	8.09	6.76	6.57	9.15	7.88	5.26	5.23	2.48	5.72
HD096482	6.57	2.10	6.32	5.62	5.54	7.45	7.42	7.64	6.31	6.19	8.48	7.56	4.96	4.92	2.12	4.82
HD100755	6.51	2.23	6.28	5.55	5.53	7.42	7.39	7.72	6.28	6.13	8.08	7.42	4.86	4.86	2.12	4.75
HD118460	6.45	2.12	6.21	5.49	5.47	7.34	7.32	7.64	6.19	6.05	8.78	7.40	4.80	4.79	2.10	4.60
HD118514	6.65	2.37	6.43	5.74	5.72	7.56	7.53	7.86	6.63	6.31	8.79	7.61	5.07	5.04	2.19	4.97
HD118678	6.99	2.41	6.69	6.08	5.98	7.89	7.84	8.10	6.80	6.71	8.99	7.88	5.51	5.32	2.61	5.91
HD118892	6.62	2.02	6.30	5.58	5.58	7.44	7.41	7.82	6.33	6.21	9.08	7.60	4.99	4.93	1.97	4.99
HD119010	6.93	2.17	6.52	5.90	5.84	7.68	7.65	8.10	6.70	6.52	8.79	7.79	5.29	5.12	2.14	5.41
HD119522	6.55	2.32	6.30	5.59	5.60	7.44	7.40	7.70	6.29	6.16	8.53	7.45	4.97	4.93	2.34	4.85
HD119591	6.58	2.58	6.47	5.78	5.72	7.63	7.60	7.76	6.56	6.29	8.73	7.59	5.05	5.02	2.49	4.80
HD119918	6.56	2.21	6.35	5.61	5.52	7.48	7.46	7.75	6.49	6.20	8.64	7.49	4.97	4.95	2.11	4.63

Table A.1 – continued

Object	Al	BaII	Ca	CrI	CrII	FeI	FeII	Mg	Na	Ni	O	Si	TiI	TiII	YII	Zn
HD119966	6.38	1.77	6.03	5.27	5.22	7.15	7.13	7.50	5.96	5.86	8.63	7.27	4.63	4.65	1.61	4.31
HD121154	6.52	1.98	6.20	5.45	5.46	7.32	7.30	7.74	6.09	6.07	8.87	7.48	4.85	4.87	1.97	4.50
HD121202	6.69	2.54	6.49	5.82	5.79	7.65	7.62	7.81	6.48	6.37	8.79	7.66	5.11	5.12	2.42	4.95
HD95455	6.75	1.91	6.27	5.49	5.58	7.34	7.32	7.71	6.24	6.16	9.00	7.58	5.03	5.07	2.06	5.01
HD95871	6.54	2.12	6.24	5.51	5.48	7.39	7.36	7.65	6.28	6.11	8.53	7.42	4.86	4.92	2.08	4.47
HD96330	6.51	2.55	6.36	5.71	5.71	7.57	7.54	7.65	6.30	6.27	8.77	7.56	5.01	5.03	2.40	4.98
HD96331	6.65	2.61	6.56	5.88	5.84	7.71	7.68	7.83	6.57	6.42	8.86	7.69	5.19	5.17	2.55	4.96
HD96440	7.20	2.63	6.78	6.27	6.20	8.01	7.96	8.37	7.07	6.84	8.90	8.11	5.72	5.46	2.80	6.33
HD96765	5.26	0.76	5.35	4.26	4.35	6.18	6.17	6.79	4.84	4.82	8.01	6.46	3.81	3.89	0.87	3.43
HD96940	6.59	2.30	6.34	5.60	5.59	7.47	7.44	7.72	6.48	6.19	8.71	7.53	4.96	5.00	2.28	4.80
HD96996	6.73	2.36	6.44	5.79	5.77	7.63	7.59	7.91	6.53	6.39	8.92	7.71	5.08	5.11	2.25	5.08
HD97144	6.72	2.60	6.60	5.96	5.90	7.78	7.74	7.88	6.64	6.49	8.85	7.75	5.26	5.20	2.49	5.14
HD97425	6.78	2.31	6.49	5.86	5.86	7.68	7.64	7.99	6.63	6.46	9.04	7.81	5.21	5.12	2.42	5.52
HD97444	6.65	2.41	6.44	5.74	5.69	7.57	7.54	7.83	6.45	6.33	8.66	7.61	5.07	5.01	2.42	4.81
HD97463	6.61	2.24	6.34	5.65	5.60	7.51	7.47	7.77	6.34	6.27	8.71	7.55	4.98	4.95	2.20	4.90
HD97750	6.92	2.25	6.56	5.99	5.91	7.72	7.69	8.06	6.84	6.60	9.18	7.96	5.30	5.05	2.24	6.14
HD98008	6.69	2.29	6.37	5.71	5.75	7.55	7.51	7.84	6.47	6.33	8.67	7.57	5.07	5.07	2.34	5.43
HD98020	6.81	2.48	6.59	5.92	5.88	7.80	7.75	7.92	6.39	6.56	8.90	7.71	5.36	5.24	2.64	5.23
HD98121	6.67	2.19	6.40	5.75	5.72	7.59	7.55	7.85	6.42	6.35	8.93	7.69	5.09	5.10	2.12	5.13
HD98507	6.76	2.51	6.54	5.89	5.83	7.72	7.68	7.97	6.64	6.46	9.00	7.76	5.20	5.17	2.42	5.07
HD98647	6.23	1.40	5.94	5.09	5.10	6.91	6.88	7.49	5.84	5.68	8.59	7.11	4.65	4.60	1.73	4.11
HD98674	6.29	1.48	5.97	5.06	5.07	6.91	6.88	7.53	5.85	5.71	8.63	7.13	4.66	4.64	1.72	4.14
HD98738	6.90	2.54	6.68	6.03	5.90	7.88	7.83	8.03	6.65	6.68	8.94	7.81	5.41	5.28	2.75	5.31
HD98761	6.50	2.26	6.32	5.61	5.61	7.46	7.43	7.67	6.30	6.21	8.76	7.48	4.99	4.96	2.23	4.84
HD98787	6.41	2.05	6.19	5.43	5.41	7.30	7.28	7.59	6.15	6.04	8.67	7.37	4.82	4.80	2.03	4.41
HD98827	6.62	2.11	6.35	5.69	5.63	7.51	7.48	7.85	6.39	6.30	8.90	7.64	4.98	4.98	2.02	5.14
HD98856	6.74	2.36	6.48	5.84	5.85	7.67	7.64	7.94	6.65	6.45	9.11	7.80	5.15	5.09	2.35	5.32
HD99551	6.72	2.50	6.53	5.89	5.82	7.71	7.68	7.90	6.58	6.47	8.97	7.75	5.20	5.17	2.52	5.26
BD-14_3284	6.31	1.59	6.05	5.16	5.22	6.95	6.93	7.58	5.91	5.74	8.69	7.17	4.76	4.70	1.98	4.35
BD-17_3277	6.58	2.42	6.44	5.77	5.75	7.62	7.58	7.81	6.37	6.35	8.76	7.59	5.12	5.11	2.51	5.04

Table A.1 – continued

Object	Al	BaII	Ca	CrI	CrII	FeI	FeII	Mg	Na	Ni	O	Si	TiI	TiII	YII	Zn
BD-22_3103	6.59	1.98	6.28	5.50	5.59	7.34	7.31	7.79	6.22	6.10	9.13	7.51	5.02	5.17	1.81	4.92

Table A.2: Abundance uncertainties

Object	Al	BaII	Ca	CrI	CrII	FeI	FeII	Mg	Na	Ni	O	Si	TiI	TiII	YII	Zn
Sun	0.10	0.07	0.11	0.08	0.04	0.10	0.08	0.11	0.08	0.08	0.04	0.07	0.13	0.24	0.07	-
HD094928	0.03	0.04	0.08	0.10	0.24	0.12	0.14	0.06	0.14	0.20	0.07	0.14	0.17	0.30	0.13	-
HD095179	0.13	0.15	0.16	0.15	0.36	0.16	0.20	0.09	0.15	0.25	0.27	0.39	0.33	0.48	0.35	-
HD096482	0.10	0.08	0.09	0.13	0.10	0.11	0.14	0.37	0.15	0.13	0.32	0.16	0.18	0.34	0.12	-
HD100755	0.12	0.05	0.09	0.08	0.09	0.11	0.11	0.05	0.14	0.14	0.91	0.37	0.16	0.28	0.10	-
HD118460	0.09	0.04	0.08	0.09	0.09	0.11	0.11	0.05	0.12	0.10	0.08	0.13	0.13	0.23	0.14	-
HD118514	0.12	0.09	0.12	0.10	0.14	0.12	0.15	0.04	0.14	0.14	0.12	0.17	0.19	0.32	0.27	-
HD118678	0.15	0.05	0.15	0.12	0.20	0.16	0.19	0.06	0.16	0.21	0.27	0.21	0.34	0.41	0.41	-
HD118892	0.09	0.06	0.10	0.09	0.20	0.13	0.14	0.07	0.13	0.14	0.13	0.18	0.20	0.29	0.20	-
HD119010	0.19	0.09	0.17	0.14	0.16	0.18	0.24	0.06	0.16	0.27	0.24	0.32	0.36	0.46	0.46	-
HD119522	0.07	0.09	0.10	0.10	0.13	0.12	0.15	0.08	0.14	0.16	0.18	0.17	0.20	0.31	0.25	-
HD119591	0.08	0.07	0.08	0.08	0.08	0.10	0.15	0.05	0.09	0.12	0.04	0.15	0.13	0.25	0.20	-
HD119918	0.10	0.06	0.08	0.08	0.07	0.10	0.13	0.04	0.10	0.10	0.03	0.13	0.14	0.20	0.11	-
HD119966	0.18	0.13	0.10	0.06	0.09	0.11	0.12	0.13	0.12	0.12	0.09	0.13	0.13	0.17	0.09	-
HD121154	0.13	0.04	0.08	0.11	0.14	0.12	0.12	0.05	0.17	0.15	0.08	0.14	0.19	0.27	0.17	-
HD121202	0.06	0.05	0.09	0.10	0.11	0.13	0.14	0.06	0.14	0.15	0.10	0.13	0.17	0.27	0.13	-
HD95455	0.10	0.08	0.09	0.09	0.17	0.14	0.16	0.36	0.13	0.20	0.13	0.16	0.20	0.33	0.34	-
HD95871	0.09	0.09	0.08	0.10	0.06	0.11	0.10	0.19	0.12	0.11	0.38	0.25	0.16	0.26	0.06	-
HD96330	0.02	0.08	0.11	0.11	0.22	0.14	0.12	0.10	0.16	0.14	0.06	0.17	0.17	0.36	0.13	-
HD96331	0.07	0.06	0.10	0.10	0.15	0.11	0.11	0.07	0.13	0.11	0.08	0.14	0.17	0.29	0.10	-
HD96440	0.25	0.15	0.25	0.17	0.28	0.22	0.25	0.09	0.25	0.34	0.49	0.40	0.44	0.56	0.46	-
HD96765	0.10	0.12	0.15	0.04	0.04	0.10	0.09	0.03	0.04	0.15	0.19	0.08	0.14	0.19	0.14	-
HD96940	0.08	0.07	0.09	0.09	0.11	0.11	0.12	0.08	0.11	0.13	0.01	0.17	0.19	0.25	0.28	-

Table A.2 – continued

Object	Al	BaII	Ca	CrI	CrII	FeI	FeII	Mg	Na	Ni	O	Si	TiI	TiII	YII	Zn
HD96996	0.06	0.10	0.12	0.14	0.12	0.14	0.15	0.04	0.21	0.15	0.11	0.21	0.25	0.41	0.27	-
HD97144	0.09	0.03	0.10	0.10	0.10	0.13	0.13	0.09	0.13	0.13	0.07	0.17	0.18	0.28	0.13	-
HD97425	0.16	0.08	0.15	0.13	0.15	0.17	0.18	0.04	0.15	0.26	0.18	0.28	0.31	0.36	0.25	-
HD97444	0.10	0.04	0.12	0.11	0.07	0.12	0.12	0.06	0.13	0.19	0.28	0.17	0.20	0.33	0.26	-
HD97463	0.12	0.06	0.11	0.12	0.14	0.12	0.12	0.10	0.15	0.16	0.12	0.15	0.19	0.32	0.18	-
HD97750	0.25	0.18	0.19	0.15	0.20	0.20	0.21	0.04	0.17	0.28	0.31	0.34	0.39	0.49	0.39	-
HD98008	0.09	0.06	0.12	0.13	0.18	0.14	0.14	0.06	0.16	0.25	0.28	0.28	0.31	0.43	0.31	-
HD98020	0.09	0.07	0.14	0.12	0.19	0.13	0.12	0.07	0.16	0.23	0.08	0.14	0.28	0.31	0.31	-
HD98121	0.07	0.09	0.12	0.11	0.13	0.14	0.07	0.06	0.17	0.18	0.10	0.20	0.23	0.36	0.30	-
HD98507	0.08	0.08	0.12	0.12	0.08	0.13	0.15	0.06	0.13	0.15	0.21	0.20	0.21	0.34	0.14	-
HD98647	0.06	0.08	0.13	0.07	0.08	0.11	0.09	0.03	0.09	0.14	0.03	0.07	0.18	0.22	0.29	-
HD98674	0.10	0.07	0.13	0.06	0.08	0.10	0.10	0.07	0.09	0.16	0.02	0.09	0.20	0.26	0.16	-
HD98738	0.07	0.08	0.14	0.11	0.19	0.13	0.14	0.10	0.14	0.17	0.15	0.13	0.24	0.33	0.26	-
HD98761	0.07	0.05	0.10	0.10	0.11	0.13	0.13	0.03	0.15	0.15	0.13	0.13	0.19	0.30	0.24	-
HD98787	0.01	0.05	0.08	0.07	0.08	0.10	0.11	0.03	0.14	0.11	0.06	0.12	0.19	0.26	0.06	-
HD98827	0.11	0.05	0.11	0.13	0.05	0.13	0.18	0.06	0.22	0.16	0.11	0.22	0.26	0.41	0.26	-
HD98856	0.13	0.07	0.12	0.14	0.15	0.15	0.16	0.01	0.17	0.19	0.13	0.26	0.30	0.38	0.28	-
HD99551	0.10	0.06	0.12	0.12	0.16	0.13	0.13	0.09	0.18	0.13	0.10	0.19	0.22	0.36	0.17	-
BD-14_3284	0.05	0.07	0.13	0.13	0.12	0.11	0.10	0.03	0.09	0.19	0.04	0.13	0.20	0.25	0.32	-
BD-17_3277	0.09	0.04	0.10	0.09	0.11	0.11	0.13	0.02	0.13	0.17	0.10	0.14	0.20	0.31	0.17	-
BD-22_3103	0.09	0.08	0.08	0.11	0.15	0.15	0.16	0.10	0.13	0.15	0.05	0.22	0.20	0.38	0.31	-

Table A.3: Atmospheric parameters

Object	T_{eff} (K)	$\log g$	[Fe/H]	V_t (km/s)
HD094928	4936	2.53	-0.23	1.41
HD095179	4747	2.40	0.07	1.50
HD096482	4912	2.37	-0.22	1.41
HD100755	4948	2.48	-0.25	1.34
HD118460	4986	2.53	-0.33	1.39
HD118514	4931	2.52	-0.11	1.38
HD118678	4945	3.05	0.21	1.02
HD118892	4819	2.36	-0.23	1.40
HD119010	4736	2.24	0.00	1.54
HD119522	4849	2.52	-0.23	1.27
HD119591	5301	2.89	-0.04	1.39
HD119918	5302	3.03	-0.19	1.27
HD119966	5025	2.43	-0.52	1.45
HD121154	4775	2.25	-0.35	1.44
HD121202	5094	2.81	-0.02	1.38
HD95455	4808	2.44	-0.33	1.45
HD95871	4963	2.52	-0.28	1.37
HD96330	5006	2.72	-0.10	0.90
HD96331	5196	3.02	0.03	1.24
HD96440	4782	2.78	0.33	1.45
HD96765	4892	2.16	-1.49	1.36
HD96940	5019	2.63	-0.20	1.36
HD96996	4799	2.42	-0.04	1.36
HD97144	5181	3.03	0.10	1.32
HD97425	4763	2.40	-0.00	1.48
HD97444	4928	2.56	-0.10	1.33
HD97463	4854	2.38	-0.17	1.39
HD97750	4682	2.29	0.04	1.70
HD98008	4640	2.25	-0.12	1.31
HD98020	4965	3.19	0.12	0.82
HD98121	4795	2.45	-0.08	1.42
HD98507	4996	2.67	0.04	1.42
HD98647	4759	2.45	-0.76	1.30
HD98674	4734	2.35	-0.76	1.23
HD98738	5062	3.19	0.20	0.92
HD98761	4839	2.61	-0.21	1.23
HD98787	5011	2.56	-0.37	1.42
HD98827	4734	2.19	-0.16	1.39
HD98856	4736	2.23	-0.00	1.39
HD99551	4918	2.61	0.03	1.37
BD-14_3284	4722	2.36	-0.72	1.31
BD-17_3277	4994	3.01	-0.05	1.00
BD-22_3103	4874	2.61	-0.33	1.49

Appendix B

References to kinematics used

Table B.1: References used for the relevant properties of our stars

Object	Coordinates	(B,V) Magnitudes	Proper Motions	Radial Velocity
HD094928	Høg et al. (1998)	Høg et al. (2000)	Høg et al. (2000)	
HD095179	Høg et al. (1998)	Høg et al. (2000)	Høg et al. (2000)	
HD096482	Høg et al. (1998)	Høg et al. (2000)	Høg et al. (2000)	
HD100755	Høg et al. (1998)	Høg et al. (2000)	Høg et al. (2000)	
HD118460	Høg et al. (1998)	Høg et al. (2000)	Høg et al. (2000)	
HD118514	van Leeuwen (2007)	Høg et al. (2000)	van Leeuwen (2007)	
HD118678	Høg et al. (1998)	Høg et al. (2000)	Høg et al. (2000)	
HD118892	van Leeuwen (2007)	Høg et al. (2000)	van Leeuwen (2007)	Gontcharov (2006)
HD119010	van Leeuwen (2007)	Høg et al. (2000)	van Leeuwen (2007)	
HD119522	Høg et al. (1998)	Høg et al. (2000)	Høg et al. (2000)	Griffin & Cornell (2006)
HD119591	van Leeuwen (2007)	Høg et al. (2000)	van Leeuwen (2007)	Gontcharov (2006)
HD119918	Høg et al. (1998)	Høg et al. (2000)	Høg et al. (2000)	
HD119966	van Leeuwen (2007)	Høg et al. (2000)	van Leeuwen (2007)	
HD121154	Høg et al. (1998)	Høg et al. (2000)	Høg et al. (2000)	
HD121202	van Leeuwen (2007)	Høg et al. (2000)	van Leeuwen (2007)	Gontcharov (2006)
HD95455	Høg et al. (1998)	Høg et al. (2000)	Høg et al. (2000)	
HD95871	Høg et al. (1998)	Høg et al. (2000)	Høg et al. (2000)	Griffin & Cornell (2006)
HD96330	van Leeuwen (2007)	Høg et al. (2000)	van Leeuwen (2007)	
HD96331	Høg et al. (1998)	Høg et al. (2000)	Høg et al. (2000)	
HD96440	Høg et al. (1998)	Høg et al. (2000)	Høg et al. (2000)	
HD96765	van Leeuwen (2007)	Høg et al. (2000)	van Leeuwen (2007)	
HD96940	Høg et al. (1998)	Høg et al. (2000)	Høg et al. (1998)	Zwitter et al. (2008)
HD96996	Høg et al. (1998)	Høg et al. (2000)	Høg et al. (2000)	
HD97144	van Leeuwen (2007)	Høg et al. (2000)	van Leeuwen (2007)	
HD97425	Høg et al. (1998)	Høg et al. (2000)	Høg et al. (2000)	
HD97444	Høg et al. (1998)	Høg et al. (2000)	Høg et al. (2000)	
HD97463	Høg et al. (1998)	Høg et al. (2000)	Høg et al. (2000)	
HD97750	Høg et al. (1998)	Høg et al. (2000)	Høg et al. (2000)	Griffin & Cornell (2006)
HD98008	van Leeuwen (2007)	Høg et al. (2000)	van Leeuwen (2007)	Gontcharov (2006)
HD98020	Høg et al. (1998)	Høg et al. (2000)	Høg et al. (2000)	Griffin & Cornell (2006)

Table B.1 – continued

Object	Coordinates	(B,V) Magnitudes	Proper Motions	Radial Velocity
HD98121	Høg et al. (1998)	Høg et al. (2000)	Høg et al. (2000)	Griffin & Cornell (2006)
HD98507	Høg et al. (1998)	Høg et al. (2000)	Høg et al. (2000)	Griffin & Cornell (2006)
HD98647	Høg et al. (1998)	Høg et al. (2000)	Høg et al. (2000)	
HD98674	Høg et al. (1998)	Høg et al. (2000)	Høg et al. (2000)	
HD98738	Høg et al. (1998)	Høg et al. (2000)	Høg et al. (2000)	Griffin & Cornell (2006)
HD98761	Høg et al. (1998)	Høg et al. (2000)	Høg et al. (2000)	
HD98787	Høg et al. (1998)	Høg et al. (2000)	Høg et al. (2000)	
HD98827	Høg et al. (1998)	Høg et al. (2000)	Høg et al. (2000)	Griffin & Cornell (2006)
HD98856	Høg et al. (1998)	Høg et al. (2000)	Høg et al. (2000)	
HD99551	Høg et al. (1998)	Høg et al. (2000)	Høg et al. (2000)	Griffin & Cornell (2006)
BD-14_3284	Høg et al. (1998)	Høg et al. (2000)	Høg et al. (2000)	
BD-17_3277	Høg et al. (1998)	Høg et al. (2000)	Høg et al. (2000)	
BD-22_3103	Høg et al. (1998)	Høg et al. (2000)	Høg et al. (1998)	

Appendix C

Kinematic properties of our stars

Table C.1: Stars' distances and their uncertainties

Object	Distance (pc)	Uncertainty (pc)
HD094928	528	42
HD095179	465	35
HD096482	659	51
HD100755	395	27
HD118460	455	31
HD118514	369	26
HD118678	380	28
HD118892	343	24
HD119010	430	33
HD119522	418	30
HD119591	387	26
HD119918	453	30
HD119966	454	32
HD121154	427	32
HD121202	366	26
HD95455	410	29
HD95871	336	23
HD96330	327	21
HD96331	287	19
HD96440	491	39
HD96765	323	23
HD96940	639	48
HD96996	624	44
HD97144	216	14
HD97425	450	35
HD97444	260	18
HD97463	423	32
HD97750	331	26
HD98008	406	32
HD98020	359	25

Table C.1 – continued

Object	Distance (pc)	Uncertainty (pc)
HD98121	497	38
HD98507	349	24
HD98647	461	35
HD98674	447	29
HD98738	496	35
HD98761	501	40
HD98787	617	42
HD98827	394	29
HD98856	389	31
HD99551	330	23
BD-14_3284	544	44
BD-17_3277	641	46
BD-22_3103	680	49

Table C.2: Space velocities and their uncertainties

Object	Space Velocities (km/s)			Uncertainties (km/s)		
	U	V	W	ϵ_U	ϵ_V	ϵ_W
HD094928	-5	25	-27	5	1	2
HD095179	39	-4	-2	3	1	2
HD096482	-10	-1	-34	3	3	3
HD100755	-4	-11	20	1	1	1
HD118460	-58	0	5	4	3	3
HD118514	-8	4	0	1	1	1
HD118678	-63	-68	-12	5	6	2
HD118892	50	-32	-34	2	1	3
HD119010	-4	9	15	2	2	2
HD119522	-47	8	0	3	2	2
HD119591	-6	-2	-16	2	2	2
HD119918	-70	-41	-17	4	5	2
HD119966	-115	-3	-33	5	4	2
HD121154	18	-17	18	2	2	2
HD121202	-37	-4	-8	2	2	1
HD95455	25	2	8	2	1	1
HD95871	-19	-12	6	2	1	1
HD96330	1	-2	-14	1	1	1
HD96331	-49	-11	-14	3	1	1
HD96440	58	7	1	5	1	2
HD96765	2	-132	57	1	2	2
HD96940	-69	10	13	5	1	2
HD96996	-97	-1	-28	8	3	4
HD97144	-2	-13	-5	1	1	1
HD97425	5	-47	-23	1	2	3
HD97444	-3	-28	0	1	1	1
HD97463	-64	-3	19	5	1	1
HD97750	-98	0	-29	8	1	1
HD98008	0	0	0	1	1	1
HD98020	-117	-129	-94	8	7	8
HD98121	28	-10	-24	6	3	3
HD98507	-29	-17	-6	2	1	1
HD98647	11	-115	-34	3	6	6
HD98674	-43	-257	-80	2	15	8
HD98738	-126	-53	-17	9	3	3
HD98761	-50	6	-23	5	2	2
HD98787	-96	-32	27	7	2	3
HD98827	37	15	-16	4	1	1
HD98856	19	-22	-11	3	2	2
HD99551	-48	-14	-7	3	1	1
BD-14_3284	3	-76	53	2	1	2
BD-17_3277	-16	-2	-18	2	1	2
BD-22_3103	-39	-64	49	5	2	2

Table C.3: Galactic orbital parameters

Object	R_{min} (pc)	R_{max} (pc)	z_{min} (pc)	z_{max} (pc)	L_z ($10^6 \cdot pc \cdot km/s$)	E ($10^3 \cdot km^2/s^2$)
HD094928	7799	12215	-614	609	-2.0	32
HD095179	6729	10151	-356	338	-1.7	25
HD096482	7829	9099	-661	656	-1.8	25
HD100755	7585	8332	-502	506	-1.7	22
HD118460	7124	9609	-399	370	-1.7	24
HD118514	7759	8981	-289	287	-1.8	24
HD118678	4234	8181	-267	266	-1.2	11
HD118892	5516	9079	-434	437	-1.5	18
HD119010	7688	9433	-466	474	-1.8	25
HD119522	7442	9811	-329	337	-1.8	25
HD119591	7673	8424	-288	286	-1.7	22
HD119918	5340	8505	-366	342	-1.4	16
HD119966	6041	11859	-699	666	-1.7	28
HD121154	6615	8433	-478	483	-1.6	19
HD121202	7399	8619	-246	246	-1.7	22
HD95455	7277	10056	-396	389	-1.8	26
HD95871	7804	8029	-270	270	-1.7	22
HD96330	7709	8942	-255	255	-1.8	24
HD96331	7192	8918	-231	231	-1.7	22
HD96440	6648	11769	-454	438	-1.8	29
HD96765	2223	8028	-1353	1319	-0.7	0.5
HD96940	7485	10993	-593	585	-1.9	29
HD96996	6805	11419	-719	739	-1.8	28
HD97144	7455	8211	-151	151	-1.7	21
HD97425	5407	8167	-358	369	-1.4	15
HD97444	6539	8067	-184	184	-1.5	18
HD97463	7187	9881	-519	523	-1.8	25
HD97750	6632	11647	-501	467	-1.8	28
HD98008	7699	9077	-288	284	-1.8	24
HD98020	2425	9307	-2573	1728	-0.8	12
HD98121	6734	9475	-451	406	-1.7	23
HD98507	7297	8093	-208	208	-1.6	20
HD98647	2631	8087	-515	525	-0.9	0.5
HD98674	427	8534	-1706	4903	0.2	22
HD98738	4630	10390	-447	384	-1.4	20
HD98761	7691	10043	-500	488	-1.8	27
HD98787	5805	9792	-739	731	-1.6	21
HD98827	7199	11425	-331	320	-1.9	29
HD98856	6492	8653	-278	277	-1.6	20
HD99551	7067	8713	-227	226	-1.7	21
BD-14_3284	4304	8084	-1306	1304	-1.2	12
BD-17_3277	7935	8754	-445	452	-1.8	24
BD-22_3103	4927	8055	-1163	1171	-1.3	14